Theoretical foundations of remote sensing for glacier assessment and mapping

Michael P. Bishop, Andrew B.G. Bush, Roberto Furfaro, Alan R. Gillespie, Dorothy K. Hall, Umesh K. Haritashya, and John F. Shroder Jr.

ABSTRACT

The international scientific community is actively engaged in assessing ice sheet and alpine glacier fluctuations at a variety of scales. The availability of stereoscopic, multitemporal, and multispectral satellite imagery from the optical wavelength regions of the electromagnetic spectrum has greatly increased our ability to assess glaciological conditions and map the cryosphere. There are, however, important issues and limitations associated with accurate satellite information extraction and mapping, as well as new opportunities for assessment and mapping that are all rooted in understanding the fundamentals of the radiation transfer cascade. We address the primary radiation transfer components, relate them to glacier dynamics and mapping, and summarize the analytical approaches that permit transformation of spectral variation into thematic and quantitative parameters. We also discuss the integration of satellite-derived information into numerical modeling approaches to facilitate understandings of glacier dynamics and causal mechanisms.

2.1   INTRODUCTION

Concerns over greenhouse gas forcing and globally increasing temperatures have spurred research into climate forcing and the responses of various Earth systems. Complex geodynamics regulate feedback mechanisms that couple atmospheric, geologic, and hydrologic processes (Molnar and England 1990, Ruddiman 1997, Bush 2001, Zeitler et al. 2001, Bishop et al. 2002). A significant component in the coupling of Earth's systems involves the cryosphere, as glaciological processes affect atmospheric, hydrospheric, and lithospheric responses (Bush 2000, Shroder and Bishop 2000, Meier and Wahr 2002). Scientists have thus recognized the significance of understanding glacier fluctuations and their use as direct and indirect indicators of climate change (Kotlyakov et al. 1991, Seltzer 1993, Haeberli and Beniston 1998, Maisch 2000).

The international scientific community is actively engaged in assessing ice sheet and glacier fluctuations at the global scale (Zwally et al. 2002, Bishop et al. 2004a, Dyurgerov and Meier 2004, Kargel et al. 2005). Glaciological studies using remote sensing and geographic information system (GIS) studies indicate that recent glacier retreat and wastage appear to be global in nature (Dyurgerov and Meier 2004, Paul et al. 2004, Barry 2006, Zemp et al. 2006). It is essential that we identify and characterize those regions that are changing most rapidly and having the most significant impact on sea level, water resources, economics, and geopolitics (Haeberli 1998). Many regions have not been adequately studied, however, and progress in scientific

understanding requires detailed analysis of parameters such as the number of ice masses, land ice distribution, changes in glacier length and volume, mass balance, dynamic response time, and ice flow dynamics.

Haeberli (2004) and Zemp et al. (see Chapter 1 of this book) indicated that a multitiered approach to this problem is required, involving measurements across environmental gradients, mass balance studies, regional assessment within different climatic zones, long-term observations of glacier length changes, and systematic multitemporal land ice inventories. This approach integrates field-based glaciological research, numerical modeling, and remote sensing and GIS-based investigations.

Careful in situ mass balance and other ground reference studies are an essential component of scientific investigations of glacier responses to climate change. However, McClung and Armstrong (1993) suggested that even detailed studies of well-monitored glaciers do not permit characterization of regional or global mass balance trends. New developments in remote sensing are required to bridge observations at a variety of scales, from the individual glacier to the global picture (Haeberli 1998, Bishop et al. 2004a, Dyurgerov and Meier 2004, Raup et al. 2007).

Glaciological research has increasingly used data from microwave, optical, and light detection and ranging (LiDAR) sensors aboard various space-based and airborne platforms. Collectively these data and new methodologies have been used to map glacier boundaries, ice flow velocity fields, and estimate other glaciological parameters such as the equilibrium line altitude (ELA) and mass balance. The availability of stereoscopic, multi-temporal, and multispectral optical satellite imagery has greatly increased our ability to assess glaciers and map their distribution (Bishop et al. 2004a). There are important opportunities and limitations associated with accurate satellite information extraction and mapping that are rooted in the fundamentals of the radiation transfer cascade.

The purpose of this chapter is to examine the fundamentals of remote-sensing science that serve as a basis for information extraction and glacier assessment. We address the primary components of radiation transfer theory and relate these to glacier dynamics and mapping. Finally, the use of satellite-derived information in numerical modeling is presented for understanding causal mechanisms responsible for ice mass fluctuations. A list of

parameters and their definitions can be found toward the end of this chapter (Section 2.9, p. 47).

2.2 RADIATION TRANSFER CASCADE

Characterization and mapping of glaciers using multispectral and multitemporal satellite imagery pose a variety of scientific and technical challenges (Bamber and Kwok 2004, Bishop et al. 2004a). Numerous physical parameters of the atmosphere and the landscape directly and indirectly govern radiation transfer (RT) processes. Radiance measured at the sensor, therefore, does not accurately represent the reflectance or emission of radiance from the landscape surface. Image spectral variation may be due to variations in atmospheric properties or topography, rather than surface material properties. The chain of RT processes, which integrates the influence of multiscale atmospheric, topographic, and surface matter–energy interactions, is complex.

For glaciologists interested in using satellite imagery, knowledge of the RT components is necessary because their influence governs spectral variability in imagery. Spectral variability due to coupled atmosphere–topography–surface interactions is problematic for applications that rely on calibrated surface radiance values. Sensor system characteristics also affect spectral variation in imagery (e.g., spatial, spectral, and radiometric resolutions). Therefore, Earth scientists must make decisions regarding radiometric calibration, image enhancement, and choice of pattern recognition algorithms. Depending upon environmental conditions, RT components may or may not significantly influence image spectral variability. Unfortunately, the influence of individual RT components (and the entire cascade) on glacier assessment and mapping has not been adequately researched.

2.2.1 Solar irradiance

The RT cascade begins with the energy output of the Sun and ultimately traces through to a sensor aboard a mobile platform. Numerous processes influence the magnitudes of emission, absorption, transmittance, and reflection of light coming from the Sun. Besides the obvious and important control of the magnitude of solar irradiance by latitude, time of day (solar elevation), and season (annual orbit and current obliquity), solar irradiance also

varies as functions of: (1) solar dynamics (magnetic, sunspot, and solar flare cycles related to the solar dynamo and convection); (2) Earth's orbital eccentricity and rotational dynamics (including the changing orbital ellipticity and distance from the Sun to the Earth, rotational obliquity, and obliquity phase with respect to Earth's orbital phase); and (3) changes in the radiation field on the Earth's surface due to atmospheric scattering and absorption (including changes in infrared opacity due to greenhouse gas and volcanic emissions). Consequently, there are changes in irradiance that are wavelength dependent ((1) and (3) above), and others that are wavelength independent ((2) above); and changes that are strictly cyclic and modulated at many frequencies ((1) and (2) above), and others that are not cyclic beyond the annual primary cycle but have either secular trends (anthropogenic greenhouse gases) or episodicity (natural greenhouse gases and anti-greenhouse volcanic aerosols). Each of these is important from the perspective of long-term climate change and glacial conditions, but from the remote-sensing image analysis perspective these variations are considered relatively insignificant because variability is either of a long period (thus having small interannual variability) or has a small amplitude.

The spectral exitance (M) of the Sun and Earth can be approximated using Planck's blackbody equation:

$$M(T_\odot, \lambda) = \frac{C_1}{\lambda^5 \left[\exp^{C_2/(\lambda T_\odot)} - 1.0\right]}, \qquad (2.1)$$

where $T_\odot$ is the temperature of the Sun, and C_1 and C_2 are the first and second radiation constants. The exoatmospheric spectral irradiance (E^0) at the top of the Earth's atmosphere can be approximated such that

$$E^0(\lambda) = \frac{M(T_\odot, \lambda)}{\pi} \frac{A_\odot}{d_{es}^2}, \qquad (2.2)$$

where $A_\odot$ is the area of the solar disk and d_{es} is the Earth–Sun distance which is a function of time. Variations in measured exoatmospheric spectral irradiance are caused by solar atmospheric interactions, and this can be compared with the blackbody approximation (Fig. 2.1). Standard exoatmospheric irradiance spectra can be used for the computation of spectral band irradiance values needed for the radiometric calibration of imagery.
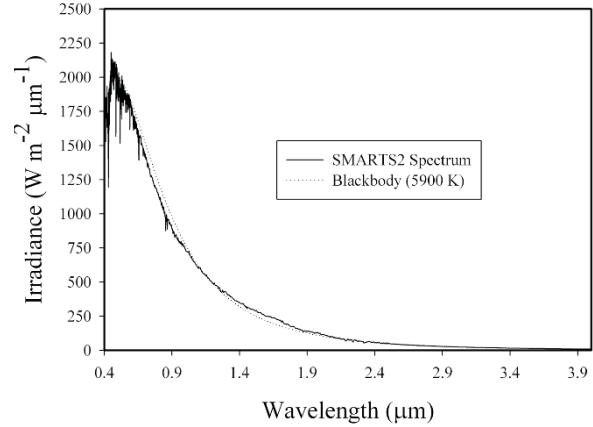

Figure 2.1. Comparison of exoatmospheric spectral irradiance from the composite SMARTS2 spectrum and a blackbody approximation. The SMARTS2 spectrum is a composite spectrum based in part on the WRC85 spectrum and balloon and satellite observations (after Gueymard 1995).

2.2.2 Surface irradiance

Radiation is transmitted through the atmosphere, and atmospheric constituents and topographic factors dictate the magnitude of radiation that reaches the surface. Surface irradiance (E) is a composite of three downward irradiance components that are wavelength (λ) dependent such that

$$E(\lambda) = E_b(\lambda) + E_d(\lambda) + E_t(\lambda), \qquad (2.3)$$

where E_b is direct beam irradiance, E_d is diffuse skylight irradiance (E_d), and E_t represents adjacent terrain irradiance. Individually and collectively these irradiance components govern a variety of surface processes such as ablation, and also dictate the magnitude of surface reflectance and emission. Depending upon environmental conditions, these components have varying degrees of influence on image spectral variability.

2.2.2.1 *Direct solar spectral irradiance*

Under cloudless skies the direct irradiance component constitutes the dominant term in equation (2.3). Much research has been conducted to model atmospheric transmittance functions accurately. The atmosphere attenuates direct irradiance primarily by gaseous absorption and molecular and aerosol scattering (Chavez 1996). These atmospheric processes are wavelength dependent and spatially and temporally controlled by changing atmospheric and landscape conditions. Total downward atmospheric transmission ($\mathbf{T}^\downarrow$) is a function of
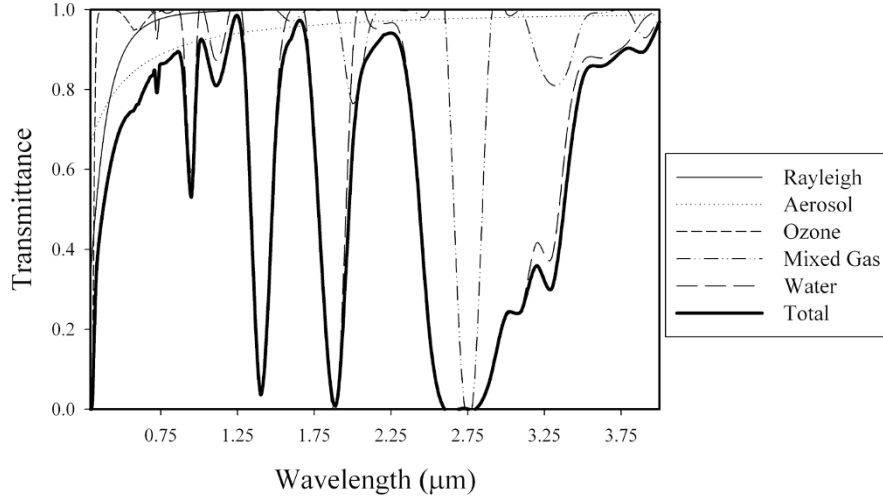
Figure 2.2. Simulated atmospheric transmittance in the shortwave spectrum at the terminus of the Baltoro Glacier near K2 in Pakistan on August 14, 2004 at 10:00 AM. Latitude: 35.692243° N; longitude: 76.165222° E; altitude: 3,505 m; solar zenith angle: 36.19°; precipitable water: 1.0 cm; ozone: 0.35 cm.

the total optical depth of the atmosphere which varies with solar zenith angle and altitude, and can be represented as

$$\mathbf{T}^{\downarrow}(\lambda) = \mathbf{T}_r(\lambda)\mathbf{T}_a(\lambda)\mathbf{T}_{O_3}(\lambda)\mathbf{T}_{gas}(\lambda)\mathbf{T}_{H_2O}(\lambda), \quad (2.4)$$

where $\mathbf{T}_r$ is Rayleigh transmittance, $\mathbf{T}_a$ is aerosol transmittance, $\mathbf{T}_{O_3}$ is ozone transmittance, $\mathbf{T}_{gas}$ is transmittance for miscellaneous well-mixed gases, and $\mathbf{T}_{H_2O}$ is water vapor transmittance. Atmospheric attenuation is highly variable with wavelength, with Rayleigh and aerosol scattering dominating at shorter wavelengths and water vapor absorption at longer wavelengths (Fig. 2.2). Direct irradiance into the surface is also governed by multiscale topographic effects. Local or microscale topographic variation is represented by the incidence angle of illumination (i) between the incoming beam and the vector normal to the ground, such that

$$\cos i = \cos \theta_i \cos \theta_t + \sin \theta_i \sin \theta_t \cos (\phi_t - \phi_i), \quad (2.5)$$

where θ_i is the incident solar zenith angle, ϕ_i is the incident solar azimuth angle, θ_t is the slope angle of the terrain, and ϕ_t is the slope–aspect angle of the terrain.

Estimation of i is possible with the use of a digital elevation model (DEM), and uncertainty in the estimate is related to the measurement scale, as subpixel-scale topographic variation is not accounted for. Values of $\cos i$ can be ≤ 0.0, indicating no direct irradiance due to the orientation of the topography. It is important to note that the incident solar geometry varies across the landscape, although this is usually assumed to be constant when working with individual image scenes (i.e., small-angle approximation). In addition, mesoscale topographic relief in the direction of ϕ_i determines if a pixel is in shadow (S). This parameter value will be 0.0 or 1.0 depending upon the presence or absence of a cast shadow, respectively. Satellite imagery acquired in rugged terrain or with relatively large solar zenith angles will exhibit cast shadows. This can be accounted for by ray tracing, shadow detection, and shadow interpolation algorithms that alter $\cos i$ values appropriately (Dozier et al. 1981, Rossi et al. 1994, Giles 2001). Local topography and shadows cast increase the global spectral variance in satellite images, with a decrease in spectral variance within shadowed areas. Collectively, the aforementioned parameters define the direct irradiance component as

$$E_b(\lambda) = E^0(\lambda)\mathbf{T}^{\downarrow}(\lambda) \cos iS. \quad (2.6)$$

In high-latitude and mountainous environments, this irradiance component can have a significant influence on glacier dynamics and image spectral variability. Local topographic variations in parameters such as slope magnitude and azimuth lead to significant variation in E_b due to ablation, supraglacial fluvial action, and supraglacial debris transport processes. Furthermore, spatial variations in slope occur as a function of altitude (Fig. 2.3). Finally, the glacier altitude range determines the
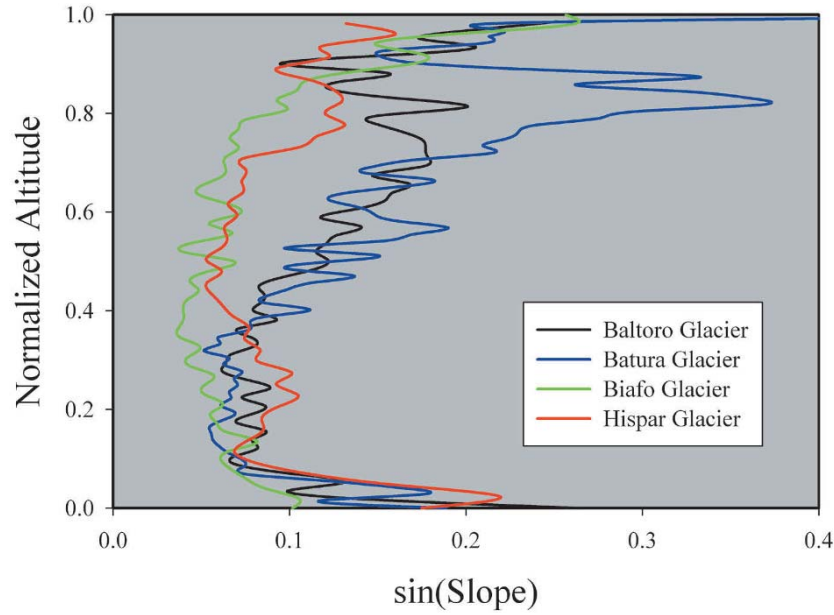
Figure 2.3. Slope–altitude plots for four alpine glaciers in the Karakoram Himalaya. Geomorphometric analysis was conducted using a SRTM 90 m digital elevation model. Average slope values were computed over a 50 m altitude interval. Different magnitudes and altitude trends are depicted. Such variation increases when a smaller altitude interval is used.

relative influence of atmospheric transmittance on this component.

In general, this component is significant and highly variable across most mountain landscapes exhibiting moderate to extreme relief (Fig. 2.4). Such variability is present in satellite imagery and usually needs to be accounted for using topographic normalization techniques. Unfortunately, many methods of topographic normalization do not effectively remove this component from satellite imagery, as they do not inherently account for multiscale topographic effects. Automated algorithms for thematic mapping are sensitive to such spectral variations caused by E_b and can classify steep slopes, cast shadows, moisture-laden debris, and surface water as the same feature. Consequently, classification accuracy can be highly variable depending upon the extent of topographic variability. Empirical spectral feature extraction (e.g., image ratioing and principal component analysis) techniques are frequently used to reduce these topographic effects, although they can still influence classification results depending upon what approach or algorithm is used.

2.2.2.2 *Diffuse skylight spectral irradiance*

Atmospheric scattering generates a hemispherical source of irradiance. This source can be simplis-

tically represented as a composite including a Rayleigh-scattered component (E_r), an aerosol-scattered component (E_a), and a ground-backscattered component (E_g) that represents inter-reflections between the landscape surface and the atmosphere, where

$$E_d(\lambda) = E_r(\lambda) + E_a(\lambda) + E_g(\lambda). \qquad (2.7)$$

Its accurate estimation is complicated by the fact that an anisotropic parameterization scheme is required. In general, diffuse skylight irradiance decreases with angular distance from the Sun. In addition, this irradiance component is also influenced by mesoscale hemispherical shielding of the topography. Consequently, only a solid angle of the sky will contribute to E_d, and this angle will change as a function of pixel location and azimuth. In general, the solid angle will increase with altitude. It is frequently referred to as the sky view factor (V_f) in the remote-sensing and energy balance literature, and can be estimated using a DEM such that

$$V_f = \sum_{\phi=0}^{2\pi} \cos^2 \theta_{max}(\phi, d) \frac{\Delta\phi}{2\pi}, \qquad (2.8)$$

where θ_{max} is the maximum local horizon angle at a given azimuth, ϕ, over a radial distance of d. In mountain environments exhibiting extreme relief
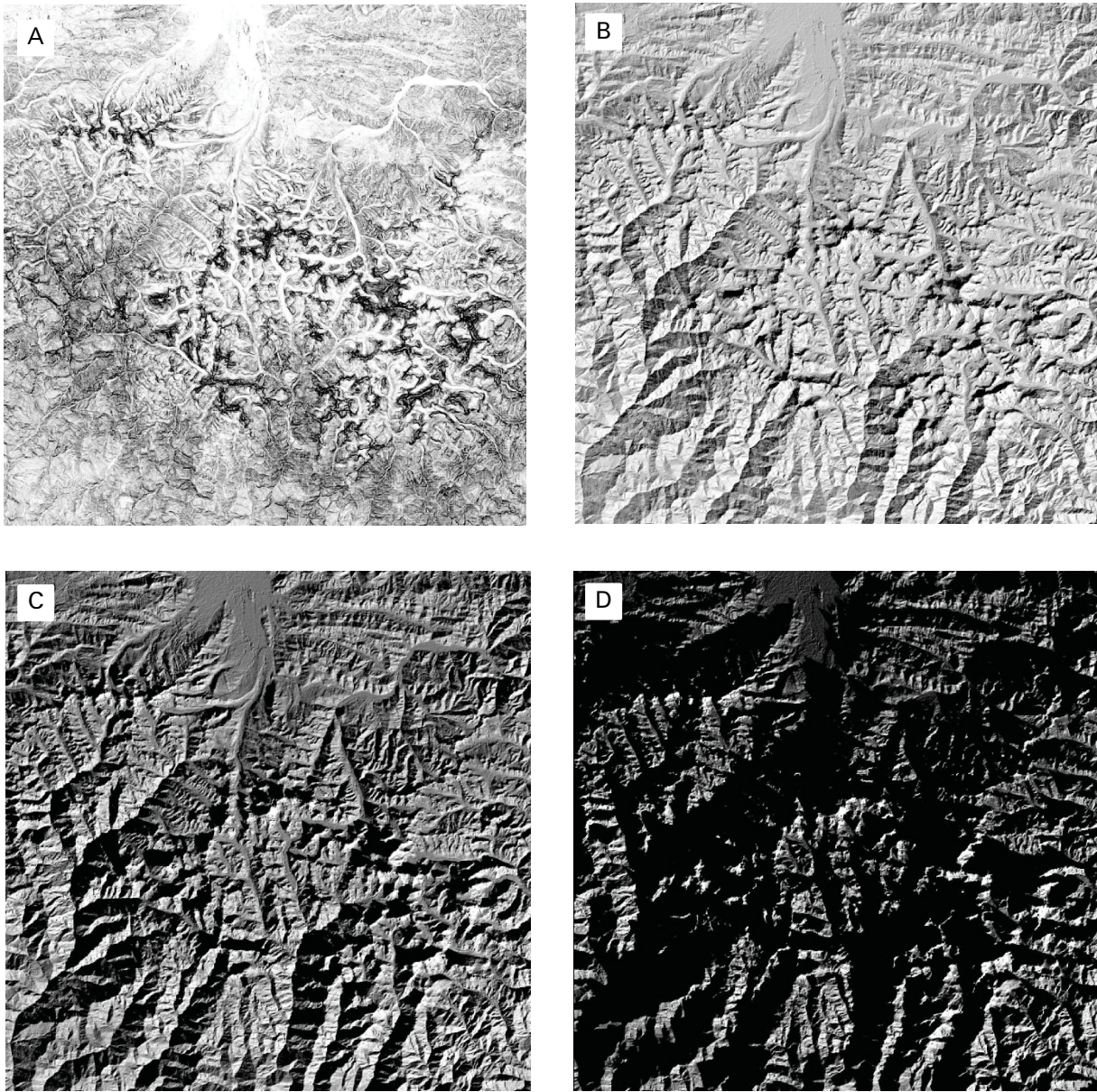
Figure 2.4. Simulations of local and mesoscale topographic influences on direct irradiance for the Mt. Everest region in Nepal. Grayscale values represent the collective magnitude of cos iS that is proportional to E_b without the influence of the atmosphere. Simulation results were obtained using ASTER GDEM data and different solar geometry. A. Solar zenith and azimuth angles of 0 and 135°, respectively. B. Solar zenith and azimuth angles of 45 and 135°, respectively. C. Solar zenith and azimuth angles of 70 and 135°, respectively. D. Solar zenith and azimuth angles of 85 and 135°, respectively.

(deep valleys), topographic shielding of skylight diffuse irradiance can be significant (Proy et al. 1989). Consequently, the sky view factor is important in environments where climate variability and glacier erosion can generate moderate to extreme topographic relief (Fig. 2.5). It will be relatively insignificant in environments with minimal topo-

graphic relief. Where significant, individual glaciers within a region receive variable amounts of energy from this component. Glacier fluctuations and mass movements alter the relief and ridgelines, such that glacier surfaces exhibit sky view variations with altitude (Fig. 2.6). Furthermore, difficulties inaccurately predicting the bidirectional reflectance distri-
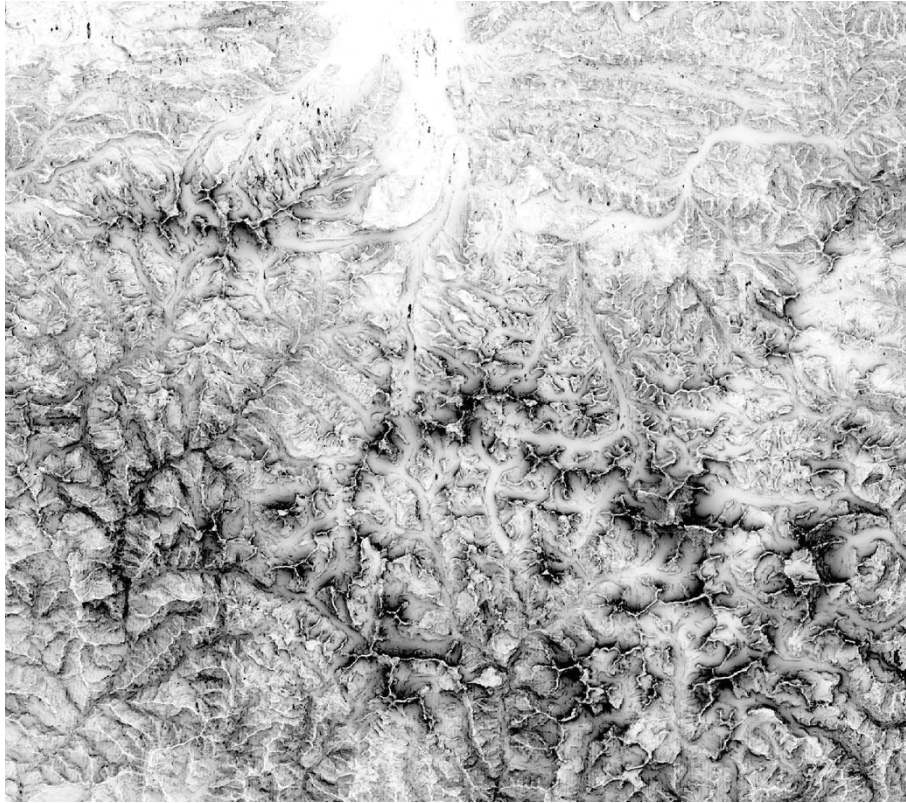
Figure 2.5. Sky view factor over the Mt. Everest region in Nepal. Dark gray tones represent relatively high topographic shielding of diffuse skylight irradiance. Lighter tones signify more diffuse skylight irradiance reaching the landscape (isotropic assumption). These results were obtained using ASTER GDEM data. Examination of the spatial patterns clearly indicates that individual glaciers receive different amounts of energy and that altitude trends exist.
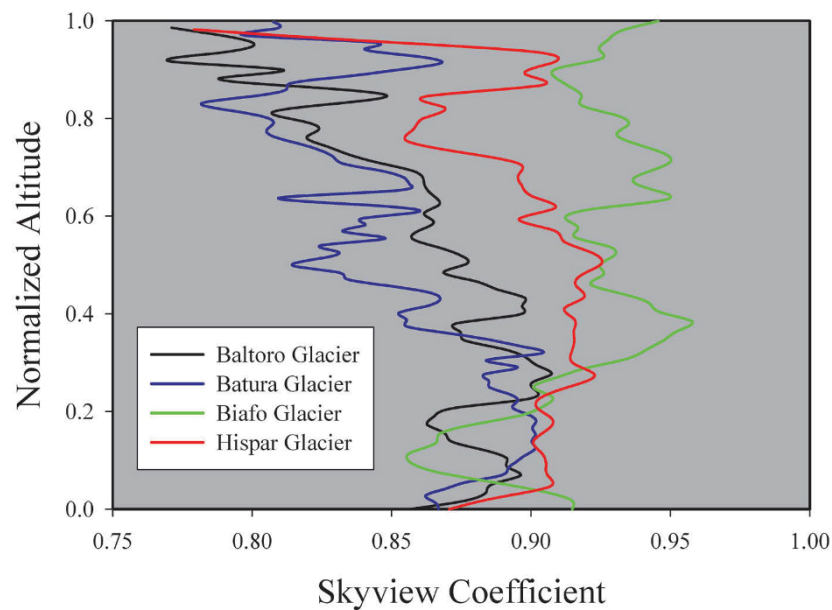

Figure 2.6. Sky view–altitude plots for four glaciers in the Karakoram Himalaya. Geomorphometric analysis was conducted using a SRTM 90 m digital elevation model. Average sky view coefficient values were computed over a 50 m altitude interval. Different magnitudes and altitude trends are depicted.

bution function (BRDF) of land cover adjacent to a particular location generates uncertainty in the estimation of the ground-backscattered component.

Such mesoscale land cover and topographic effects on this irradiance component are present in satellite imagery, although visual detection is difficult due to the dominance of direct irradiance and surface reflectance. In addition, lower spatial frequency components are difficult to detect and reduce, as topographic normalization approaches do not effectively address this irradiance component.

More research is required to determine what the magnitude of this topographic effect is on image spectral variability. However, the magnitude can be deemed as potentially crucial in certain limited but important cases. The diffuse skylight irradiance component generally is of the order of 5–10% of direct irradiance, as any photographer knows, or as gauged from the ASTER VNIR-band DN values in typical mountain shadows compared with directly illuminated terrain. In heavily shadowed zones (such as in northern-aspect cirque glaciers in the Northern Hemisphere), the diffuse skylight component can approach the direct solar beam in its importance to the energy budget. The sky view factor in rough terrain, such as in Himalayan valleys, can then account for blocking up to half, or even more, of the diffuse skylight. In general, relative to direct beam irradiance, diffuse skylight and skyview shielding each become more important as relief increases (e.g., in narrow canyons) and as latitude increases (MacClune et al. 2003).

2.2.2.3 *Adjacent terrain spectral irradiance*

The irradiance components E_b and E_d interact with the terrain and land cover biophysical characteristics to generate an adjacent terrain irradiance component (E_t).

This irradiance component is not generally considered in remote-sensing and energy balance studies because it is assumed that its magnitude is relatively minor and it is a difficult parameter to estimate accurately. A first-order approximation was formulated by Proy et al. (1989) and assumes that reflected surface radiance is Lambertian. It is then possible to estimate the radiance received at any pixel by accounting for the geometry between two pixels (p_1 and p_2) such that

$$L_{12} = \cos \theta_1 \left(L_2 \cos \theta_2 \left[\frac{A_p}{d^2} \right] \right), \qquad (2.9)$$

where L_{12} represents the radiance received at p_1 from the luminance of p_2 (L_2), θ_1 and θ_2 are the angles between the normal to the terrain and the direct line of sight from p_1 to p_2, A_p is the pixel area (p_2), and d represents the distance between p_1 and p_2.

This equation can be used to estimate E_t for any pixel by integrating over all of the pixels whose slopes are oriented towards a pixel of interest and where the line of sight is not blocked by the topography. High-altitude and extreme local relief areas can exhibit a strong adjacent terrain irradiance component due to highly reflective features such as snow and vegetation.

2.2.3 Surface reflectance

The magnitude of reflected and emitted radiance at the surface is determined by the conservation of energy, and is expressed by Kirchhoff's law as

$$\rho(\lambda) + \alpha_a(\lambda) + \mathbf{T}(\lambda) = 1.0, \qquad (2.10)$$

where, ρ, α_a, and $\mathbf{T}$ represent reflectance, absorption, and transmission, respectively. For opaque objects $\mathbf{T} = 0.0$. Therefore, spectral reflectance can be approximated as

$$\rho(\lambda) = \frac{M(T_s, \lambda)}{E(\lambda)}, \qquad (2.11)$$

where T_s is surface temperature. Given a Lambertian surface, which reflects radiation equally in all directions, reflected surface spectral radiance (L) can be computed as follows:

$$L(\lambda) = \rho(\lambda) \left(\frac{E(\lambda)}{\pi} \right). \qquad (2.12)$$

Satellite imagery can be used to estimate surface radiance and reflectance, although atmospheric correction is required. In general, this can be approximated as

$$L(\lambda) = (L^0(\lambda) - L_p(\lambda)) / \mathbf{T}^{\uparrow}(\theta_r, \lambda), \qquad (2.13)$$

where L^0 is at-satellite measured radiance, L_p is additive path radiance from the atmosphere, and $\mathbf{T}^{\uparrow}$ is upward total atmospheric transmittance that is a function of the reflected zenith angle (θ_r) and wavelength.

2.2.3.1 *Bidirectional reflectance distribution function and albedo*

Unfortunately, the Lambertian assumption is not valid on glaciers (see Chapter 3 of this book by

Furfaro et al.), and the anisotropic nature of surface reflectance must be characterized to permit accurate assessments of surface albedo and ablation. Numerous parameters influence reflectance anisotropy which is characterized by the bidirectional reflectance distribution function (f_r). It is defined as the ratio between reflected radiance and units of incoming surface irradiance. It is represented as

$$f_r(\theta_i, \phi_i, \theta_r, \phi_r, \lambda) = \frac{L(\theta_i, \phi_i, \theta_r, \phi_r, \lambda)}{E(\theta_i, \phi_i, \lambda)}, \quad (2.14)$$

where ϕ_r is the reflected azimuth angle. This function characterizes bidirectional reflectance for all combinations of incident and viewing angles.

In satellite remote sensing, a distinct, but closely related, parameter is the bidirectional reflectance factor (R_r). This parameter is frequently utilized because it characterizes directional reflectance in a convenient unitless form. It is formally defined as the ratio between the reflected radiance in any particular direction, and the radiance that would be reflected into the same direction by an ideal Lambertian surface, illuminated by the same source with the same incident geometry. It can be shown (Feng et al. 1993) that f_r and R_r are related by the simple relationship

$$R_r(\theta_i, \phi_i, \theta_r, \phi_r, \lambda) = \pi f_r(\theta_i, \phi_i, \theta_r, \phi_r, \lambda). \quad (2.15)$$

This quantity is becoming a standard product for satellite-based radiometers capable of acquiring angular measurements of reflected radiation from the landscape over a scene (e.g., multiangle imaging spectroradiometer, MISR, and the polarization and directionality of Earth reflectance instrument, POLDER; see Diner et al. 1999). The values of R_r can be greater than one, for example, due to specular reflection.

The aforementioned reflectance parameters are closely related to a parameter generally called surface albedo (α). It is a spectrally and hemispherically integrated surface parameter that significantly governs surface energy balance. We distinguish between two types of albedo. Planar surface albedo (α_{psa}) is formally defined as follows:

$$\alpha_{psa}(\theta_i, \phi_i, \lambda) = \int_0^{2\pi} \int_0^{\pi/2} \mu_r f_r(\theta_i, \phi_i, \theta_r, \phi_r, \lambda) \, d\theta_r \, d\phi_r, \quad (2.16)$$

where $\mu_r = |\vec{n} \cdot \vec{\Omega}_r|$, $\vec{n}$ is the normal vector, and $\vec{\Omega}_r = (\theta_r, \phi_r)$. It is the ratio between reflected and incoming radiation integrated over the hemisphere. The integration removes the dependence of albedo

from the reflection geometry and therefore it is a global quantity.

Spherical surface albedo (α_{ssa}) is obtained by averaging planar albedo over the irradiance hemisphere. It is defined as

$$\alpha_{ssa}(\lambda) = \frac{1}{\pi} \int_0^{2\pi} \int_0^{\pi/2} \mu_i \alpha_{psa}(\theta_i, \phi_i, \lambda) \, d\theta_i \, d\phi_i, \quad (2.17)$$

where $\mu_i = |\vec{n} \cdot \vec{\Omega}_i|$ and $\vec{\Omega}_i = (\theta_i, \phi_i)$. It is important to point out that for any surface in the cryosphere, Kirchhoff's law of conservation during matter–energy exchange (assuming local thermodynamic equilibrium) dictates that emissivity and albedo are related by the simple relationship $\varepsilon_s(\lambda) = 1 - \alpha_{ssa}(\lambda)$, respectively.

2.2.4 Surface emission

Upward longwave surface spectral radiance $L_\uparrow$ can be approximated as

$$L_\uparrow(\lambda) = \varepsilon_s(\lambda) \frac{M(T_s, \lambda)}{\pi}. \quad (2.18)$$

Emissivity is a parameter that characterizes the efficiency with which the surface radiates energy compared with an ideal cavity or blackbody, for which $\varepsilon_s = 1$.

If ε_s is known for at least one reference wavelength, as it is for snow and ice (Fig. 2.7), surface temperature can be computed as

$$T_s = \lambda C_2^{-1} \left[\ln\left(\varepsilon_s(\lambda) C_1 \pi^{-1} \lambda^{-5} L_\uparrow^{-1}(\lambda) + 1 \right) \right]^{-1}. \quad (2.19)$$

Since T_s is invariant with λ, it is then possible to calculate the emissivity spectrum if multispectral data are available. For most remote-sensing studies, however, other factors must be considered, complicating the inversion for T_s (i.e., atmospheric effects). Consequently, at-satellite measured longwave spectral radiance $L_\uparrow^0$ can be represented as

$$L_\uparrow^0(\lambda) = \mathbf{T}^\uparrow(\lambda) \left(\varepsilon_s(\lambda) \frac{M(T_s, \lambda)}{\pi} + (1 - \varepsilon_s(\lambda)) L^\downarrow(\lambda) \pi^{-1} \right) + L_p^\uparrow(\lambda), \quad (2.20)$$

where $\mathbf{T}^\uparrow$ is upward longwave atmospheric transmissivity. Downwelling longwave spectral irradiance is $L^\downarrow$, and $L_p^\uparrow$ is upwelling longwave atmospheric path radiance. $L^\downarrow$ is reflected from the surface, which is usually taken to be a perfect diffuse (Lambertian) reflector, in which case reflectivity is simply given by $(1 - \varepsilon_s(\lambda))$ according to Kirchhoff's law.
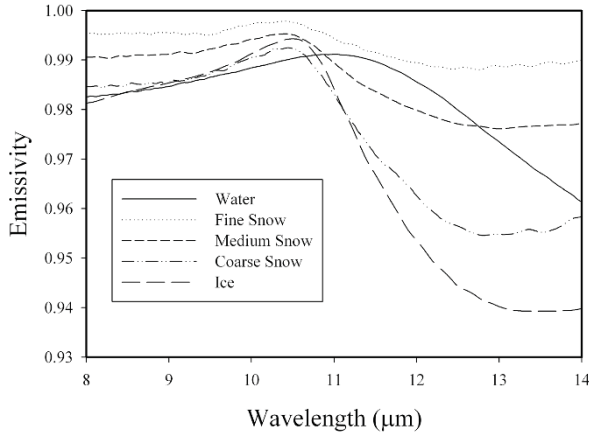
Figure 2.7. Thermal emissivity of water, snow, and ice. The uncertainties of emissivities estimated from ASTER are about ±1.5%. Spectral coverage does not extend to long enough wavelengths to exploit the spectral differences of snow and ice fully. The emissivities calculated from reflectivity data measured by J.H. Salisbury at Johns Hopkins University (*http://speclib.jpl.nasa.gov / scripts /lib/asp/WaterResp.asp*), using Kirchhoff's Law. The emissivity of natural rough surfaces will be increased and spectral contrast lowered due to multiple reflections.

Finally, eq. (2.20) must be adjusted for topographic effects in order to have predictive capabilities for rough terrain. To first order, the emitted term is unaffected by terrain. Terrain, however, shields longwave irradiance from the atmosphere, although this is substituted by longwave adjacent terrain irradiance, as the surrounding terrain surface is generally warmer than the sky. These terrain influences can be estimated using a DEM and eq. (2.8) to modify the previous equation such that

$$L_\uparrow^0(\lambda) = \mathbf{T}^\uparrow(\lambda)\left(\varepsilon_s(\lambda)\frac{M(T_s,\lambda)}{\pi} + (1 - \varepsilon_s(\lambda))\right.$$

$$\times \left.\left(L^\downarrow(\lambda)\pi^{-1}(1 - V_f) + 2\pi L_t^\downarrow(T_t,\lambda)V_f\right)\right)$$

$$+ L_p^\uparrow(\lambda), \tag{2.21}$$

where $L_t^\downarrow$ is longwave irradiance from the adjacent terrain and T_t is the temperature of the adjacent terrain. Here it is assumed that the adjacent terrain and sky are isothermal. These assumptions are unrealistic, the terms multiplying $(1 - \varepsilon_s(\lambda))$ are better regarded as spatial averages over the sky hemisphere, and T_t is better regarded as a variable, especially for work on snowfields and glaciers, where the terrain may be bare and have a strongly different temperature than the snow. Parameter V_f

can be called a "form factor" in radiosity theory, where it describes the solid angle subtended by one surface element viewed from another.

For many snow or ice studies at high altitude, the radiosity effect is relatively small because the reflectivity of the snow is low in the longwave part of the spectrum. For example, if the snow surface is at 273 K and the adjacent bare hillsides ($\varepsilon_s = 0.95$) are at 303 K, and 10% of the sky hemisphere is shielded, the apparent temperature of the snow surface is increased only ~ 0.2 K. Only if the rocks are warmer or substitute more of the sky hemisphere is this a measurable effect in imagery (e.g., ASTER).

It is noteworthy that the atmospheric terms $L^\downarrow$ and $L_p^\uparrow$ are controlled by the vertical distributions of gases and temperature, with water vapor playing a key role. Parameter $L^\downarrow$ is heavily weighted by contributions from the lower atmosphere, but $L_p^\uparrow$ is strongly influenced by absorption due to gases throughout the atmospheric column, a process that is independent of temperature.

For terrain with low relief, once atmospheric variables and emissivities are known, T_s is estimated according to eq. (2.19). In areas of high relief, however, especially if hillsides adjacent to snowfields or glaciers are bare of snow, it may be necessary also to know the temperature and emissivity of adjacent surfaces in order to solve for T_s. Here it is best to use a temperature/emissivity separation algorithm to estimate both temperatures and emissivities from ASTER images (Gillespie et al. 1998). Although noise-equivalent change in temperature (evaluated at 300 K) for ASTER is <0.3 K, temperatures can typically be recovered only within ±1 K, due to compounded uncertainties in atmospheric variables, calibration coefficients, and assumed emissivity.

2.3 SURFACE–ENERGY INTERACTIONS

2.3.1 Snow

Use of optical, infrared, and microwave sensors provides synergy that may allow extraction of important snowpack properties to improve our understanding of matter- energy interactions in a snowpack (e.g., Hall et al. 2005). Snow-covered areas can generally be detected most accurately using optical data, and augmented by microwave data when darkness and clouds prevail. Snow albedo can be estimated using data from the reflective part of the spectrum. Snow water equivalent,
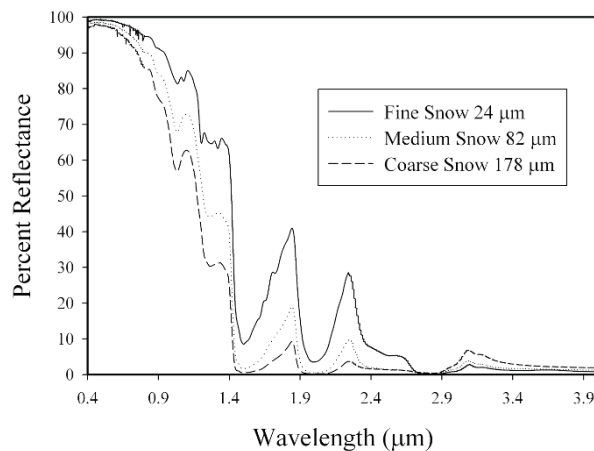
Figure 2.8. Reflectance of snow with different effective particle size. Reflectivity data obtained from the ASTER Spectral Library (*http://speclib.jpl.nasa.gov*), which was collected at the Johns Hopkins University IR Spectroscopy Lab. The laboratory spectra here may be compared with idealized radiative transfer–based computed spectra of pure ice shown in Figure 3.4 of this book (Furfaro et al.'s chapter).

however, is an important hydrologic parameter, and can be estimated using microwave wavelengths that penetrate the snowpack or emanate from the ground.

One of the first observations made in the study of early satellite images of the Earth's surface was coverage of some surfaces by high-albedo snow. Surface albedo is the ratio of upwelling reflected flux to downwelling incident irradiance. New, fine-grained snow cover reflects more than $\sim 80\%$ of incident solar radiation, while older, coarse-grained and/or melted and refrozen snow tends to reflect far less radiation (Fig. 2.8), especially when it has been covered by soot/dust or volcanic ash. Broadband albedo is reflectance across the reflective part of the solar spectrum. Broadband albedo decreases when grain size increases as the snow ages (Choudhury and Chang 1979), and melting causes snow grains to grow and bond into clusters (Dozier et al. 1981, Warren 1982, Dozier 1989).

With the onset of surface melting and associated grain size increases, near-infrared reflectance decreases dramatically (e.g., Fig. 2.8; Warren and Wiscombe 1980, Warren 1982). The near-infrared albedo of snow is very sensitive to snow grain size while visible albedo is less sensitive to grain size, but is affected by snow impurities. For example, for the case of just 3 ppm of soot in snow, see the computed spectra in Figure 3.6 (Furfaro et al.'s chapter), and compare also with their computed Figure 3.4 for

pure snow and our Figure 2.8 for actual snow. Warren and Wiscombe (1980) considered the case for snow containing aerosol impurities. Effective snow grain radii typically range in size from $\sim 50\,\mu m$ for new snow, to 1 mm for wet snow consisting of clusters of ice grains (Warren 1982). Snow albedo may decrease by $>25\%$ within just a few days as grain growth occurs (Nolin and Liang 2000). The albedo of a snow cover, if it is thin, is also influenced by the albedo of the land, especially when vegetation extends above the snow surface.

Snow albedo can be approximated over large areas by deriving the linear relationship between the brightest snow-covered areas such as arctic tundra and the darkest snow-covered forest in a scene. Albedos can be assigned 0.80 and 0.18, respectively, as did Robinson and Kukla (1985) using Defense Meteorological Satellite Program (DMSP) imagery (0.4–$1.1\,\mu m$). Linear interpolation was then performed to derive albedo. Today, snow albedo can be estimated directly from satellite data using the Moderate-resolution Imaging Spectroradiometer (MODIS) (e.g., Klein and Stroeve 2002, Schaaf et al. 2002).

A near-surface global algorithm has been developed to map snow albedo using MODIS data. In deriving albedo, atmospherically corrected MODIS surface reflectance in individual MODIS bands for snow-covered pixels located in nonforested areas is adjusted for anisotropic scattering effects using a discrete ordinates radiative transfer model (DISORT) and snow optical properties (Klein and Stroeve 2002). Currently in the algorithm, snow-covered forests are considered to be Lambertian reflectors. The adjusted spectral albedos are then combined into a broadband albedo measurement using a narrow-to-broadband conversion scheme developed specifically for snow (Nolin and Liang 2000, Klein and Stroeve 2002). Thus derived, a near-global snow albedo product is available as part of the suite of MODIS snow cover products and has been since February 2000 (Hall and Riggs 2007).

In the thermal region, eq. (2.21) is underdetermined, and a solution for T_s requires independent information, especially for atmospheric conditions. For ASTER images, these data have come from NCAR/CIRES reanalysis data from radiosonde probes of water, temperature, and pressure profiles. These profiles are converted to $L^{\downarrow}$ and $L_p^{\uparrow}$ using the MODTRAN radiative transfer model. For work on snow and ice, emissivity is generally measured in the laboratory or taken from a spectral library. For

snow and ice, terrain irradiance is less important in the thermal infrared than in the visible, near-infrared, and shortwave infrared, because snow and ice have reflectivities <5% between wavelengths of 8 and 12 μm (Fig. 2.7). Nevertheless, steep, bare rock walls above glaciers will have a measurable effect, all the more important because the reflectivity of snow and ice differ at longer wavelengths, with snow a factor of two or more less reflective than ice. Estimation of snow and ice temperatures is best made at ~10.5 μm, because the emissivities are about the same and no distinction between them is necessary in advance.

2.3.2 Glaciers

Glacier surfaces are composed of a variety of materials that exhibit unique reflectance patterns. High spatial variability in reflectance results from variations in the debris cover, ice properties, surface moisture content, and snow and firn properties. For example, in ablation areas, debris cover lithology, depth, and surface roughness significantly affect ablation and moisture content, while reflectance from ice surfaces is dominated by properties such as air bubble and englacial load characteristics. Furthermore, centimeter-scale roughness from cryoconite holes in ice can produce additional spectral reflectance variation. In the accumulation area, reflectance is controlled by the magnitude of metamorphism of ice crystals, firn density, and moisture content (Rees 2006). Collectively, surface matter and property variation, multiscale topographic effects, and variations in solar geometry result in anisotropic reflectance (Greuell and de Wildt 1999).

Greuell and de Wildt (1999) measured and empirically modeled the anisotropic reflection of the radiation of melting glacier ice on the Morteratschgletcher Glacier in Switzerland. They found that anisotropy increases with longer wavelengths (Fig. 2.9), with increasing θ_i, and with decreasing α. Wavelength dependence can be explained due to changes in the absorption coefficient of ice with wavelength (Grenfell and Perovich 1981). A higher absorption coefficient produces lower surface albedo, which also dictates the shorter effective pathlength of photons through the ice. Statistically, a shorter pathlength governs the number of scattering events, which leads to better preservation of the angular distribution of photons in multiple scattering events, which is described by the scattering phase function f_p. The amount of anisotropy increases with decreasing θ_i for snow-covered glaciers, as forward-scattered photons penetrate more deeply for small zenith angles, and photons are more evenly distributed (Warren et al. 1998). Lower albedo is caused by surface impurities and debris that can sometimes increase surface meltwater, which subsequently affects the absorption coefficient in a positive feedback.

The relationships between fundamental radiometric parameters and various properties of the glacier surface can be made explicit by considering the basic physical laws that describe the conservation of energy for photons being transported across particulate media. As photons reach the glacier surface they enter the ice–snow–firn medium and are subject, in principle, to the same absorption-scattering mechanisms that occur in the atmosphere. Nevertheless, glacier surface properties are
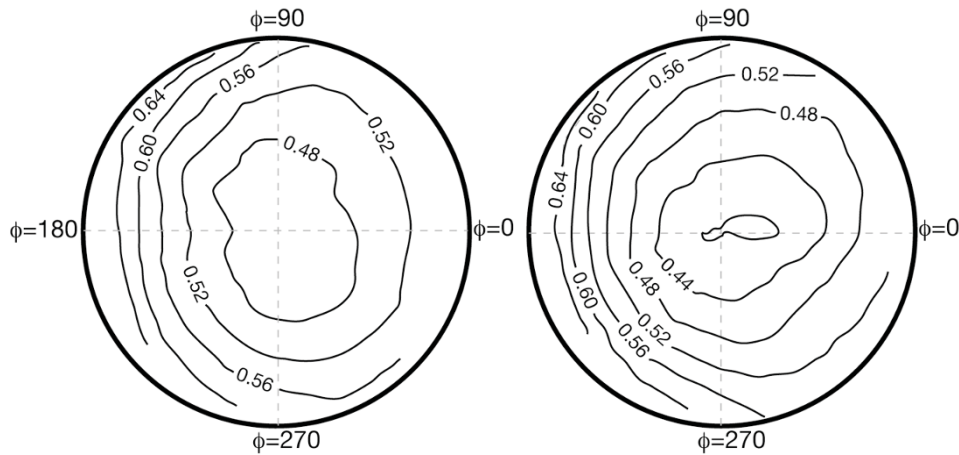

Figure 2.9. Broadband BRDFs measured over melting glacier ice: (left) Thematic Mapper band 2, $\theta_i = 50°$, $\alpha = 0.52$; (right) Thematic Mapper band 4, $\theta_i = 50°$, $\alpha = 0.50$ (modified after Greuell and de Wildt 1999).

very different than atmospheric properties. Using first principles, physical models can be derived to compute the spectral radiance leaving the glacier surface, as well as to compute the BRDF/BRF parameters to provide knowledge of surface behavior. In the specific case of glaciers, the theoretical computation of the BRDF/BRF is generally accomplished by assuming the surface to be a homogeneous, plane-parallel particulate layer of ice or snow, and solving the corresponding radiation transfer equation (RTE). If the optical properties (scattering and absorption coefficient and f_p) of ice or snow are known, the conservation of photons in the appropriate phase space yields the linearized Boltzmann equation such that

$$\mu \frac{\partial}{\partial \tau} L(\tau, \mu, \phi) + L(\tau, \mu, \phi)$$
$$= \frac{\omega}{2} \int_{-1}^{1} \int_{0}^{2\pi} f_p(\cos \Theta) L(\tau, \mu', \phi') \, d\mu' \, d\phi'. \quad (2.22)$$

Here we assume that radiance is a function of only one spatial dimension (depth) as well as a function of inclination ($\mu = \cos \theta_i$) and azimuthal angle (ϕ_i). Optical thickness (τ) is related to thickness (h) via the extinction coefficient $\sigma_{ext}(\tau = \int_0^h \sigma_{ext}(h) \, dh)$. Single-scattering albedo, ω, is the ratio between scattering and extinction, while f_p describes the probability that a photon moving in direction $\vec{\Omega}_0$ is scattered in the direction $\vec{\Omega}$. Moreover, f_p depends on $\Theta = \vec{\Omega}_0 \cdot \vec{\Omega}$ (i.e., the angle between incoming and scattered photons).

Eq. (2.22) must be equipped with appropriate boundary conditions and solved numerically to compute L. Various numerical techniques are available to solve the RTE and include the iterative solution of the Ambartsumiam's integral equation (Mishchenko et al. 1999), adding–doubling technique (Hansen and Travis 1974), converged discrete ordinates method (Ganapol and Furfaro, 2008), and analytical discrete ordinates method (Siewert 2000). Areal and intimate mixtures of snow, ice, and debris can be modeled using radiative transfer theory (see Chapter 3).

The computed radiance can be directly used to evaluate the theoretical BRDF and/or BRF for different types of glaciers. Such parameters can be employed to study the effect of particle size, shape, and orientation of ice crystals on the reflected signal. Examples of a RT-computed BRF for ice particle models are shown in Fig. 2.10. Mishchenko et al. (1999) considered three ice models including: (1) particles with a highly irregular, random fractal

shape (i.e., snow), (2) homogeneous ice spheres, and (3) regular hexagonal ice crystals. Reflected intensities are displayed in polar plots: each column corresponds to an ice model (1, 2, and 3); the rows show BRF as a function of incident angle (the stars on the plots indicate the inclination of the incident photon beam). Clearly, the scattering phase function for the particle type has a marked effect on the BRF. While small differences are perceived when looking at the nadir direction across models, large variations exist in other directions. Note that for model 1, the BRF has less structure/features than model 3 (i.e., degree of anisotropy). Indeed, a regular hexagonal ice model has a more structured phase function than a randomly oriented, fractal-like model.

2.3.3 Water

Increases in temperature and high ablation produce significant quantities of meltwater that eventually can form supraglacial and proglacial lakes. The reader is directed to the following chapter by Furfaro et al. for further theoretical treatment of this topic of radiative transfer in glacial waters. The interaction between light and water is dictated by the same first principles describing photon propagation in particulate media. The physics of interaction are described by eq. (2.22) which formalizes the conservation of photons either absorbed or scattered or eventually reemitted in any direction. Naturally, there are key differences and similarities that markedly distinguish the transport of light in water from any other medium. For example, in the case of water–light interaction, the visible part of the spectrum, 400–700 nm, is of interest because it is related to biological activity, and is the region where optical transmission is the largest. From a modeling point of view, glacier meltwater lakes can be modeled using the so-called plane-parallel approximation. Here it is generally assumed that the water column is layered and incident radiation is uniform over the surface.

Optical properties play a critical role in determining the behavior of reflected light as collected by observing sensors. Such properties (i.e., absorption, refraction, and scattering) are generally difficult to characterize. Water is the primary compound that also potentially incorporates organic and inorganic matter. These constituents exhibit high spatio-temporal variability in concentration. Multiple components are generally present within the water, and it is assumed that the absorption and scattering
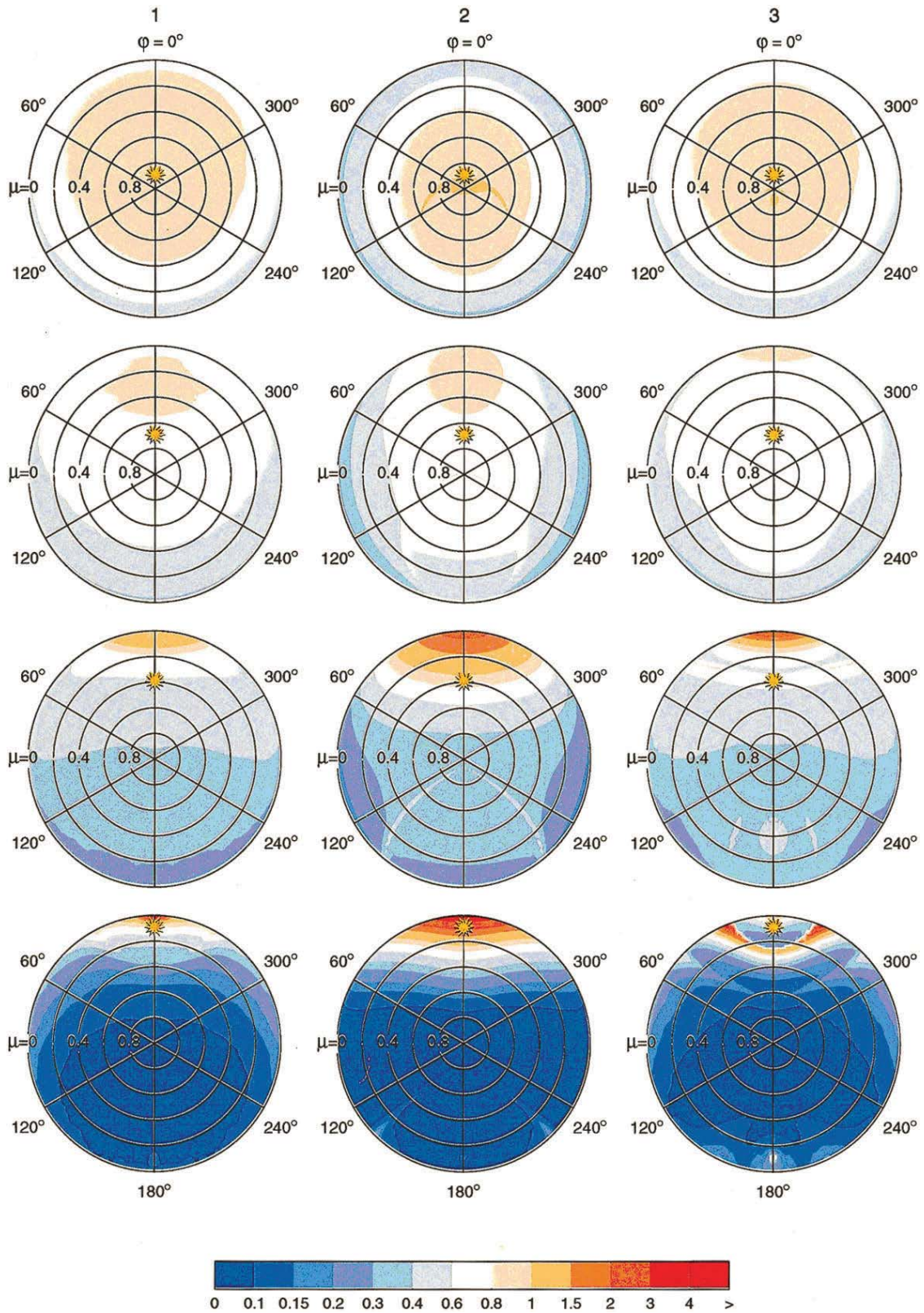
Figure 2.10. Two-angle reflected intensity as a function of inclination ($\mu = \cos\theta_v$) and azimuth (ϕ_v) for three different snow models. The yellow star indicates the incident solar zenith angle (from Mishchenko et al. 1999).

coefficients of individual, optically active constituents are additive. We can distinguish between clear water and turbid meltwater. For water, optical properties are primarily determined by the concentration of suspended detritus. Indeed, there is a formal correlation between absorption (a_p) and scattering (b_p) coefficients and concentration of particles (C) which can be described as follows (Prieur and Sathyendranath 1981):

$$a_p(\lambda) = 0.06 A'_p(\lambda) C^{0.602}, \qquad (2.23)$$

$$b_p(\lambda) = 0.5 B'_p(\lambda) \left[\frac{550}{\lambda}\right] C^{0.62}. \qquad (2.24)$$

A'_p and B'_p range between 0.12 and 0.45 m^{-1}. For turbid water, the optical properties (including spectral variation in reflectance) are strongly influenced by mineral particle concentration. Suspended sediments/particles tend to be scatterers rather than absorbers. Nevertheless, the mineralogical composition of the particles can also be a factor especially in the case of iron-rich sediments that feature strong absorption bands.

Turbid glacier meltwaters exhibit an extremely forward-peaked scattering, with a peak forward to backscatter ratio on the order of 10^6. Scattering has been modeled using a forward-peaked phase function derived by experimental data (Petzold 1972) and analytical models such as the Fournier–Fourand model (Fournier and Fourand 1994).

2.4   COMPLICATIONS

The previous sections outline the complexity of radiation transfer and the relatively large number of variables that influence sensor spectral response. Information extraction from satellite data is predicated upon isolating specific variance components of the radiation transfer cascade. This frequently requires radiometric calibration to account for the significant variables that cause spectral variation. In practice, accurate information necessary to utilizing physical models to reduce unwanted variation caused by the atmosphere or the topography is not readily available, and Earth scientists typically rely upon empirical approaches to reduce or isolate spectral variation.

A classic example for glacier assessment includes topographic normalization of satellite imagery. Glaciologists rarely account for all the irradiance components and viewing geometry related to topography. Instead, empirical procedures such as ratioing or principal component analysis is used to reduce topographic effects. This is usually effective for thematic mapping applications, although quantitative estimation of surface parameters requires more detailed insight and treatment of the radiation transfer cascade.

2.5   SPACE-BASED INFORMATION EXTRACTION

Satellite imagery contains a wealth of information for assessing the Earth's cryosphere (Bishop et al. 2004a). Extracting these signals and pertinent glacier information can be challenging. New techniques and analytical approaches are frequently required to identify and transform spectral variation into thematic and quantitative parameters. We focus here on the type of information that can be extracted from satellite imagery.

2.5.1   Snow cover

Snow cover mapping can be accomplished at a variety of temporal and spatial scales with high accuracy. Today, satellite-borne instruments provide detailed information on snow cover in the visible, infrared, and microwave parts of the electromagnetic spectrum on a daily basis at a global scale. In 1997, the Interactive Multi-sensor Snow and Ice Mapping System (IMS) began to produce operational products daily at a spatial resolution of about 25 km, utilizing a variety of satellite data (Ramsay 1998). Improvements in the spatial resolution of the IMS product in February 2004 resulted in snow maps at 4 km resolution. In June 1999, NOAA/NESDIS ceased producing weekly maps, replacing them with the daily IMS product (Ramsay 1998).

Since February 24, 2000 the Moderate Resolution Imaging Spectroradiometer (MODIS) sensor has been providing daily snow maps at a variety of different temporal and spatial resolutions (Hall and Riggs 2007). MODIS is a 36-channel imaging spectroradiometer that was first launched as part of NASA's Earth Observing System (EOS) program on December 18, 1999 on the Terra spacecraft. A second MODIS was launched on May 4, 2002 on the Aqua spacecraft. Snow maps are available from MODIS to serve the needs of local, regional, and global modelers and are provided at 500 m, 5 km, and 25 km resolution, and as daily, weekly, or

monthly composites, including fractional snow cover and albedo (Hall and Riggs 2007). Snow cover maps are also routinely generated using higher resolution satellite imagery coupled with a variety of pattern recognition methods. This results from the good statistical separability between snow reflectance and the reflectance of other land-cover classes.

2.5.2 Ice sheets

Using Advanced Very High Resolution Radiometer (AVHRR) data and, more recently, MODIS data, it is possible to achieve daily mapping of the Greenland Ice Sheet. With microwave data, most cloud cover is not an issue, but there are also many complexities in terms of what is being observed, and the use of data from optical wavelengths provides a wealth of information about ice sheet characteristics including surface temperature and albedo.

Comiso (2006) has shown, using monthly AVHRR-derived, surface temperature maps, that much of the Arctic has been undergoing a steady warming since 1981, including a $1.19°C$ per decade increase over Greenland. More recently, Hall et al. (2006) provided improved temporal and spatial detail using 5 km resolution MODIS surface temperature maps that show the temperature distribution in the various facies of the ice sheet. The glacier facies (Benson 1996) are delineated based on snow and ice characteristics, and subsequently changes of the facies boundaries over time can be correlated with ice sheet mass balance. For example, using surface temperature maps, an increase in the elevation of the boundary between the percolation and dry-snow facies could be monitored over time to reveal associated temporal changes in ice sheet mass balance.

Satellite data (AVHRR) have also been used to map changes in albedo over the Greenland Ice Sheet during the spring and summer months (Knap and Oerlemans 1996, Nolin and Stroeve 1997, Stroeve et al. 1997, Comiso 2006). Recently, Stroeve et al. (2006) have used MODIS data to analyze the accuracy of daily albedo measurements from MODIS of the Greenland ice sheet.

Surface albedo over the Greenland Ice Sheet has also been measured using data acquired by the EOS Multiangle Imaging Spectroradiometer (MISR) instrument. MISR images the surface using nine discrete, fixed angle cameras, one nadir viewing and four viewing angles in forward and aftward directions along the spacecraft track. Compared with in situ measurements at five different sites, the surface albedo derived from two different methods using MISR data showed good agreement (Stroeve and Nolin 2002). Although the atmosphere is relatively thin over the ice sheet, atmospheric attenuation is significant in the visible and near-infrared wavelengths.

2.5.3 Alpine glacier mapping

Glaciers are known to be directly and indirectly sensitive to climate variations, and a top priority of assessing climate change is to monitor and understand glacier fluctuations at a variety of scales (Haeberli et al. 1998, Bishop et al. 2004a, Kargel et al. 2005, Haeberli 2004), and to quantify the errors (Hall et al. 2003). This requires information on changes in glacier distribution.

The nature and uncertainty of information extracted from satellite imagery is strongly related to sensor characteristics. Relatively high spatial resolution and good image geometric fidelity is required to resolve smaller alpine glaciers and glacier features. High spatial resolution also permits spatial analysis of glacier surfaces, such that ice flow and structural characteristics can be assessed and mapped (e.g., Bishop et al. 1998). In addition, scene coverage should be large enough to enable regional analysis.

Spectral resolution controls spectral differentiation of glacier surfaces from other landscape features. Glacier surface reflectance is governed by ice structures and the concentration of air bubbles (Winther 1993), variations in grain size of snow/firn (Kääb 2005b), surface water content (König et al. 2001), and dust and/or supraglacial debris.

In general, the near and shortwave infrared regions of the spectrum are important for snow and ice mapping, and many different satellite sensors can be used to map alpine glaciers that have minimal debris cover. Atmospheric conditions, however, such as cloud cover and aerosol influences can affect spectral response. The anisotropic nature of surface reflectance is also an issue, as multiscale topographic effects can significantly influence interpretation (Bishop et al. 2004a, b). Existing spectral bandwidth characteristics, however, make it difficult to map debris-covered glaciers as spectral differentiation between rocks and sediment on and off glaciers is relatively poor (Bishop et al. 2001, 2004b, Paul et al. 2004). Other issues include radiometric resolution and sensor gain which can lead to sensor

saturation over snow and ice, and repeat coverage which affects change detection studies.

Alpine glacier mapping can be accomplished using a variety of methods, each with advantages and disadvantages. The most common approach used worldwide is based on cursor tracking, which is commonly known as on-screen manual digitization from a false-color composite (FCC), and/or spectrally enhanced imagery (i.e., ratios or principal components). This approach takes advantage of spectral variations of landscape features; it is labor intensive and fraught with difficulties, as results are necessarily dependent upon geographic knowledge and experience of the analyst. Glacier boundaries can easily be misinterpreted. Other techniques for glacier boundary delineation include the image ratio approach (e.g., Hall et al. 1989, Paul et al. 2002), supervised and unsupervised classification (e.g., Gratton et al. 1990, Aniya et al. 1996), and the use of artificial neural networks (e.g., Bishop et al. 1999). Most of these techniques require image preprocessing and work reasonably well for clean ice, but they tend to fail for debris-covered glaciers. Details regarding mapping glaciers using satellite spectral data are covered in Chapter 4.

Change detection studies have produced estimates of retreat rates and changing mass balances for alpine glaciers around the world. The crucial factors for temporal analysis include selecting suitable images, identifying change categories, and using appropriate change detection algorithms (Lu et al. 2004). Space-based glacier change detection studies include monitoring of variations in terminus position (retreat, advance, and/or surge), downwasting, snow line, debris cover, exposed glacial area, supraglacial lake fluctuations, and mass balance. Some of these parameters may be interrelated, such as glacier terminus position and mass balance changes (Haeberli and Hoelzle 1995), and changes in supraglacial debris thickness and cover and glacier surface downwasting. Paul et al. (2004) indicated that many glaciers are currently downwasting instead of retreating. It is important to note, however, that methods to measure annual mass balance are still being studied (Khalsa et al. 2004).

2.5.4 Debris-covered glaciers

Mapping debris-covered glaciers is notoriously difficult (Williams et al. 1991, Bishop et al. 2001). Different approaches have been attempted, and the use of topographic information in addition to multispectral imagery is generally required. Paul et

al. (2004) developed an automated approach to map debris-covered glaciers using slope and curvature derived from a DEM and neighborhood analysis. Bishop et al. (2001) used a scale-dependent automated object-oriented approach which classifies debris-covered glaciers and surface features such as ice cliffs and moraines. These examples demonstrate the feasibility of automated mapping of debris-covered glaciers, although the results are highly dependent upon the quality and resolution of the DEM, and on the sophistication of the approach. Research indicates that integrated data fusion approaches can be well suited to effectively make use of spectral data and multiple forms of topographic information. Details regarding DEM generation and geomorphometry are covered in Chapter 5.

Data on the supraglacial debris cover characteristics of glaciers is sorely needed, as debris cover exerts a tremendous influence on the ablation process (Nakawo and Rana 1999). Previous research indicates a complex relationship between debris cover thickness and ablation, where debris cover can either retard or enhance ablation rates depending on the spatial variability in debris lithology and thickness (Loomis 1970, Mattson et al. 1993). Remote-sensing studies indicate that debris cover thickness can be highly variable (Bishop et al. 1995), and field research indicates a general pattern of greater debris depths towards the terminus and lateral edges of many alpine glaciers (e.g., Gardner and Jones 1993). These patterns are caused by mass movement and ice flow dynamics that transport debris to the terminus and edges via horizontal and vertical advection. Increases in surface ablation and glacier surface downwasting overtime, and sometimes increases in delivery of debris to the glacier by landslides and other mass movements, can result in increases in the percentage of debris cover. Conversely, acceleration of flow due to positive mass balance or surging sometimes can move debris to terminal and lateral moraines and partially clear away debris from much of the glacier surface. Consequently, field or remote-sensing assessment of debris cover patterns and debris depth variability is essential for estimating ablation, glacier mass balance, glacier sensitivity to climate change, and water supply from the ablation area.

Satellite imagery can be used to map variations in supraglacial lithologies. For example, Nakawo et al. (1993) were able to differentiate and map areas of granitic and schistose debris over the Khumbu

Glacier in Nepal. In other areas in the Himalaya, the predominant debris lithologies can be mapped and include differentiation of: (1) granitic and black metasediment debris in the Hindu Kush, (2) granodiorite, weathered granodiorite, and black metasediments in the Hunza Himalaya, and (3) granite, gneiss, and black and red metasediment debris in the Karakoram Himalaya. Such capabilitites also exist for debris-covered glaciers in Alaska and the Andes Mountains. Difficulties in automated mapping and lithologic characterization of debris result from spectral variation caused by glacier topography, moisture-laden debris, and supraglacial lakes. This is especially the case when debris lithology is predominately mafic in composition and numerous features exhibit relatively low reflectance throughout the spectrum. Whereas finely intermixed debris and ice (areal or intimate mixtures) can be assessed quantitatively by analysis of satellite imagery, and areas of continuous debris can be mapped, debris thickness is very difficult to assess by remote sensing.

Research regarding the estimation of ablation under a debris layer indicates that the surface temperature of debris may be used to estimate thermal resistance (Nakawa and Young 1981, Nakawo et al. 1993). This may work accurately only if the debris is relatively thin, as it sometimes is. However, some efforts to assess debris thicknesses, or to assess the edges of glaciers using thermal data over debris-covered glaciers, may be thwarted or rendered partially effective if the debris cover is thick or is of uncertain grain size. Grain size and lithology-dependent thermal conductivities may vary significantly, causing uncertainty in the results of these approaches. More troubling, if debris is more than a few centimeters thick, thermal conductive equilibrium is not obtained; rather, temperatures can be controlled by the thermal inertia of the debris (which includes heat capacity as well as thermal conductivity), basically causing internal storage and release of heat in the debris. Current models inadequately address this problem.

Thermal inertia variations are primarily caused by variations in thermal conductivity which is primarily controlled by particle size distribution. A surface composed of large rock boulders will have a relatively high thermal inertia, while smaller particles and fine-grained dust will have lower thermal inertia. Diurnal temperature variations will not be influenced by debris conditions deeper than one diurnal thermal skin depth. Debris depth temperature profiles have been documented to exhibit non-

linear variation, presumably due to thermal inertia. Moisture conditions, including evaporative cooling on debris surfaces, also must be accounted for, but there is no easy way to do this using remote-sensing data. Though thermal data provide information related to glacier mapping, great care must be exercised when using satellite temperature estimates to assess debris depths.

2.5.5 Snow line and ELA

The transient snow line (TSL) is the sometimes irregular edge between snow and bare glacier ice on a glacier. Snow line elevation is strongly controlled by latitude, topography, and regional climatic systems that govern irradiant flux, precipitation, and snow accumulation. Seasonal variations in the altitude of the TSL are significant. It can be estimated using satellite imagery and a DEM. The highest altitude of the TSL during the ablation season is often considered to be equivalent to the glacier equilibrium line altitude (ELA), the demarcation between a glacier's accumulation and ablation zones (Carrivick and Brewer 2004, Kulkarni et al. 2004).

Given the paucity of regional mass balance information, there is an urgent need to produce estimates of mass balance for individual glaciers over extensive regions. Space-based assessments of the TSL permit this, as field-based mass balance estimates can be calibrated with the accumulation area ratio (AAR) (Kulkarni et al. 2004). The AAR is the ratio between the accumulation area and total glacier area. When mass balance data exist for several glaciers, the functional form of the relationship between the AAR and the specific mass balance can be used within a region, given numerous assumptions (Khalsa et al. 2004).

For example, Kulkarni et al. (2004) estimated the specific mass balance of 19 glaciers in the Himachal Pradesh region of the India Himalaya, based upon glaciological mass balance data obtained from 1982 to 1988. A strong regression relationship was obtained and used with the LISS-III sensor of the Indian Remote Sensing Satellite (Fig. 2.11). It is important to recognize that significant uncertainties exist and are related to: (1) inability of the glaciological method to adequately account for the spatial variation in ablation and accumulation; (2) variability in topographic conditions that govern shortwave and longwave irradiance fluxes, and therefore ablation and ELA variation; and (3) spatial variations in accumulation rates due to variations in the
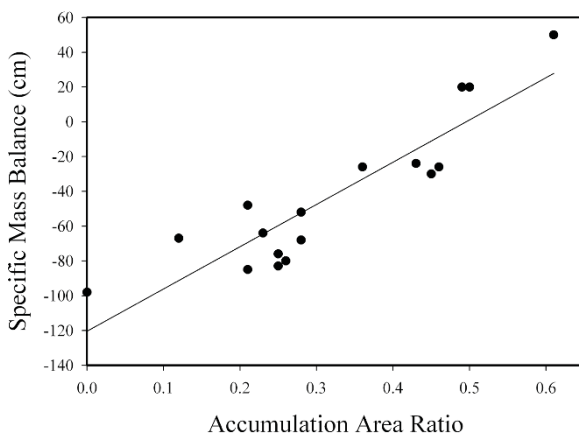
Figure 2.11. Relationship between the accumulation area ratio and the specific mass balance for Shaune Garang and Gor Garang glaciers in the India Himalaya. Reproduced from data in Kulkarni et al. (2004).

influence and/or coupling of regional climate systems. In addition, glacier hypsometry and regional topographic variations must also be considered.

Nonetheless, a variety of statistical methods have been developed and tested to estimate ELAs using reflectance and topographic data. The most common include the AAR approach, the area–altitude balance ratio (AABRs), the area–altitude balance index (AABI), and median elevation of a glacier (MEG) (Meierding 1982, Furbish and Andrews 1984, Kulkarni 1992, Benn and Evans 1998, Osmaston 2005). Other popular methods to reconstruct previous ELAs include maximum elevation of lateral moraines (MELM) and various toe-to-head-wall altitude ratios (THAR) (Nesje 1992, Torsnes et al. 1993). Several studies carried out for snow line assessment from the last glacial maximum (LGM) using these methods were reviewed by Mark et al. (2005).

2.5.6 Ice flow velocities

The velocity field of a glacier is an important glaciological parameter that governs a variety of processes, and controls glacier geometry and extent. Ice velocities can be highly variable, and diurnal and annual fluctuations have been observed (e.g., Jansson 1996, Nienow et al. 2005). Microwave data and optical imagery are commonly used to estimate ice flow velocities. With the latter, multitemporal satellite imagery permits the generation of an average horizontal ice flow velocity field over the period of separation of the images.

A basic technique for extracting the velocity field is based on feature tracking, where identifiable features on the glacier (e.g., crevasses or snow dunes) are tracked in images acquired at different times. Feature-tracking research has focused primarily on large polar glaciers and ice streams (Kääb 2005a, Scambos et al. 1992), although this technique can be applied to smaller alpine glaciers (Kääb 2005a, b). It works particularly well for glacier surfaces where the ice surface structure remains unchanged over time. In general, after preprocessing the imagery to enhance moving features, a computer program searches for correlation matches at many points in the image and, for each one, produces a subpixel estimate of the horizontal velocity based upon the correlation field. Rapidly changing alpine glacier surfaces can potentially pose a challenge to this approach in terms of uniform velocity fields, as surface features can change dramatically due to rapid mass movement and transport of debris, ablation changing debris cover conditions and ice structures, supraglacial lake development, evolution, and drainage, and non-linear spatial variations in ice flow direction. Furthermore, spectral saturation and heavy debris cover can limit the production of usable correlations. Consequently, more research into developing new methods to account for supraglacial reflectance variability is warranted. Details regarding feature-tracking methodologies are covered in Chapters 4 and 5.

Kääb (2005a) identified the need for developing a set of comprehensive goals and strategies for inventorying ice flow dynamics. Ice flow is a fundamental process of glaciers, and the spatial and temporal variability in ice flow fields can provide us with new insights into understanding the relationships between climate, glaciers, and mountain geodynamics. For example, Kääb (2005a) used ASTER data to estimate glacier flow velocities in the Bhutan Himalaya. Alpine glaciers in the Himalaya may be classified as summer or winter accumulation type, receiving precipitation predominately from the monsoon or the westerlies. They receive precipitation from both, however, and understanding the influence of source partitioning and changes in partitioning over time is an important topic that has not been adequately addressed. We might expect spatial variations in ice flow velocity to be strongly associated with ice flux (i.e., snow accumulation). An example of this is shown in Fig. 24.6, where higher velocities are associated with the glaciers on the north side, where basal conditions and

orography lead to velocities of up to $200 \, \text{m yr}^{-1}$. On the south side, higher ablation and rainfall produces thermokarst features, more supraglacial lakes, and lower velocities.

2.6 NUMERICAL MODELING

The integration of remote sensing–derived parameters and numerical modeling which has been previously discussed represents a more sophisticated approach to the study of glacier dynamics and the interpretation of causal mechanisms. Information generated from satellite imagery and DEMs can be used to establish boundary conditions, estimate input parameters, and constrain simulations. We briefly discuss the significance of numerical models for understanding glacier fluctuations.

2.6.1 Climate modeling

While mapping and monitoring the present conditions of ice sheets and alpine glaciers is a fundamental and necessary task, predictions of future mass balances must rely on knowledge of what the climate will likely be sometime in the future. Such knowledge can only come from numerical modeling of the climate system. In addition, general circulation models (GCMs) can be used for paleoclimate studies in which direct comparisons with proxy climate data recovered from various regions may be made.

The equations that are used to describe the evolution of the atmosphere are based on the hydrodynamic equations of motion combined with thermodynamic laws. They conserve mass, momentum, and energy. The momentum equations that express the three-dimensional force balance may be written as follows in the coordinates of x (longitude), y (latitude), and p (pressure, which is used as a vertical coordinate rather than height z):

$$\frac{\partial U}{\partial t} + U\frac{\partial U}{\partial x} + V\frac{\partial U}{\partial y} + W\frac{\partial U}{\partial z}$$
$$= -\frac{1}{\rho_a}\frac{\partial p}{\partial x} + 2\Omega V \sin \varphi + 2\Omega W \cos \varphi + F_x, \quad (2.25)$$

$$\frac{\partial V}{\partial t} + U\frac{\partial V}{\partial x} + V\frac{\partial V}{\partial y} + W\frac{\partial V}{\partial z}$$
$$= -\frac{1}{\rho_a}\frac{\partial p}{\partial y} - 2\Omega U \sin \varphi + F_y, \quad (2.26)$$

$$\frac{\partial W}{\partial t} + U\frac{\partial W}{\partial x} + V\frac{\partial W}{\partial y} + W\frac{\partial W}{\partial z}$$
$$= -\frac{1}{\rho_a}\frac{\partial p}{\partial z} - g + 2\Omega U \cos \varphi + F_z, \quad (2.27)$$

where U, V, and W are the zonal, meridional, and vertical wind speeds, respectively; ρ_a is atmospheric density; p is air pressure at latitude φ; Ω is the rotation rate of the Earth; and F_x, F_y, and F_z are frictional terms whose form varies depending on what processes are resolved by the model. Sub-grid-scale motions (i.e., unresolved motion) will be parameterized in some fashion and included in these terms. On the left-hand side of eqs. (2.25), (2.26), (2.27), the second, third, and fourth terms represent three-dimensional advection. The first term on the right-hand side is the acceleration produced by pressure gradient forces, followed by Coriolis acceleration terms. Gravitational acceleration, g, is seen in the vertical momentum—eq. (2.27). For synoptic-scale atmospheric flow it is quite common to simplify and use the hydrostatic approximation, which retains only two of the terms:

$$\frac{\partial p}{\partial z} = -\rho_a g. \quad (2.28)$$

The hydrostatic approximation forces the vertical pressure gradient to be balanced by buoyancy. This approximation is good for atmospheric motion on the global scale, and means that the full set of equations is easier to solve numerically. However, it comes at a price: convection in the atmosphere is precluded under the hydrostatic assumption because vertical acceleration is assumed to be zero. (There can still be vertical motion as a result of mass continuity and horizontal convergence/divergence, however.) The benefits of assuming hydrostatic balance are therefore tempered by the need to parameterize convection and cloud formation processes in some fashion.

An equation of state is required and the assumption that the atmosphere is an ideal gas is quite a good one for normal ranges of atmospheric temperatures and pressures:

$$p = \rho_a R T_a, \quad (2.29)$$

where T_a is the temperature of the atmosphere and R is the dry-air gas constant.

Invocation of energy conservation for an ideal gas with a specific heat at constant pressure of c_p and a thermal expansion coefficient α_{te} yields the

following prognostic thermodynamic equation:

$$\frac{\partial T_a}{\partial t} + U\frac{\partial T_a}{\partial x} + V\frac{\partial T_a}{\partial y} + W\frac{\partial T_a}{\partial z}$$
$$= \frac{\alpha_{te}T_a}{\rho_a}\left(\frac{\partial p}{\partial t} + U\frac{\partial p}{\partial x} + V\frac{\partial p}{\partial y} + W\frac{\partial p}{\partial z}\right) + \frac{H}{c_p}, \quad (2.30)$$

where H is an energy term to which latent, sensible, and radiative heating contribute. Mass conservation is expressed in these coordinates by

$$\frac{\partial \rho_a}{\partial t} + U\frac{\partial \rho_a}{\partial x} + V\frac{\partial \rho_a}{\partial y} + W\frac{\partial \rho_a}{\partial z}$$
$$= -\rho_a\left(\frac{\partial U}{\partial x} + \frac{\partial V}{\partial y} + \frac{\partial W}{\partial z}\right). \quad (2.31)$$

In addition to these dynamic/thermodynamic equations, an expression for the conservation of water is required and is usually written in terms of specific humidity, q:

$$\frac{\partial q}{\partial t} + U\frac{\partial q}{\partial x} + V\frac{\partial q}{\partial y} + W\frac{\partial q}{\partial z} = E_v - P, \quad (2.32)$$

where E_v is the rate of evaporation and P is the rate of precipitation.

Eqs. (2.25) through (2.32)—using either (2.27) or (2.28)—represent seven equations for the seven unknowns U, V, W, T_a, p, ρ_a, and q. These equations, in one form or another, are at the core of all modern general circulation models.

The seemingly innocuous heating term on the right-hand side of eq. (2.30) contains a wealth of physics wherein contributions from remote sensing can be made. Radiative transfer through the atmosphere is computed for both shortwave and longwave radiation and a particular atmospheric composition (which can change in its content of aerosols and water vapor). The divergence/convergence of radiative fluxes produces cooling/heating terms through H. Latent heating during precipitation/convection events is computed according to the particular convective parameterization used and also contributes to H, as does the sensible heating associated with parameterized convective motions.

Surface temperature is a crucial element and is computed from a surface energy balance that takes into account sensible and latent heat fluxes, net shortwave and net longwave radiation. Implicit in the calculation is surface albedo. Some general circulation models incorporate land surface parameterization schemes in which the land surface can respond to climate forcing and hence albedo can change according to land cover dynamics. It is common to assume the surface to be a graybody such that albedo does not depend on wavelength. Historically, the albedo of large ice masses was fixed at a particular value and only snow cover could change. It is now known that the albedo of glaciers has significant seasonal variation due to meltwater and surface debris. Crude parameterizations have been developed to address this seasonality, but remote sensing is required to obtain atmospheric and land surface information that better characterizes the spatiotemporal complexities of these important parameters.

2.6.2 Energy balance modeling

Together with accumulation, the overall factor that governs the mass balance of a glacier is surface energy balance. Surface energy budget is composed of a variety of processes that determine the magnitude of ablation (ice mass losses due mainly to melting and sublimation). It has been demonstrated that the spatial and temporal variability of ablation is high in mountain regions given altitude ranges, topographic conditions, and debris cover variability (Bishop et al. 1995, Arnold et al. 2006). The classical method based on positive degree day estimation of melting provides a crude proxy to part of the energy balance formulation given below, but it is directly related only to sensible heat. The degree day method implicitly assumes that the other terms scale in some way with sensible heat, such that there is an empirical relation between degree days and melting. This is not strictly true, and can be highly inaccurate and misleading, and so the use of the positive degree day method is decreasing.

It is generally acknowledged that three-dimensional numerical modeling of the energy budget is required to characterize the spatiotemporal complexity of numerous processes that affect ablation, especially on alpine glaciers. Consequently, input of spatiotemporal data from remote sensing and GIS is needed to reduce the uncertainties associated with key parameters and processes such as albedo, irradiance flux, and turbulent fluxes.

A physically based approach for estimating ablation requires assessment of energy fluxes. The components of an energy flux can be represented as:

$$Q_N + Q_H + Q_L + Q_G + Q_R + Q_M = 0 \quad (2.33)$$

where Q_N is net radiation, Q_H is sensible heat flux, Q_L is latent heat flux (Q_H and Q_L are referred to as turbulent heat fluxes), Q_G is ground heat flux, Q_R is the sensible heat flux supplied by rain, and Q_M is the

energy used for melting snow and ice. Positive quantities represent energy gains while negative magnitudes indicate energy loss at the surface.

Ablation rate (M_a) estimates generated from energy balance modeling are generally deemed reliable (Hock 2005). Ablation is computed as:

$$M_a = \frac{Q_M}{\rho_w L_f}, \qquad (2.34)$$

where ρ_w is the density of liquid water and L_f is the latent heat of fusion.

All of the energy flux components are time variable. They include momentary fluctuations related to weather; diurnal, annual, and longer term cycles; and long-term trending related to global climate change. Ablation and mass balance assessments are most usefully and commonly integrated over the annual cycle. However, comparison of winter and summer mass balances also provides important information about ice throughput and the timescales of glacier dynamical responses to perturbations.

2.6.2.1 Net radiation

The net radiation component represents the balance between incoming and outgoing energy absorbed and emitted by the surface. It is characterized and modeled as shortwave (0.15–4.0 μm) and longwave (4.0–120 μm) radiation fluxes, and is usually the dominant energy source. Net radiation is regulated by numerous processes and key parameters that represent atmospheric, topographic, and surface properties.

The radiation balance can be computed as:

$$Q_N = E(1 - \alpha) + L^\downarrow + L_t^\downarrow + L^\uparrow, \qquad (2.35)$$

where E is surface irradiance, $L^\downarrow$ is total longwave sky irradiance, and $L^\uparrow$ is total emitted longwave radiation.

Albedo α can be estimated using satellite imagery. It is also possible to measure albedo in the field and empirically model the relationship between measured albedo and surface radiance. This parameter, however, does vary over time, and numerous approaches to modeling albedo have been developed (Arendt 1999).

Longwave radiation can be characterized using numerous parameterization schemes. In general, incoming longwave irradiance ($L^\downarrow$) can be represented as:

$$L^\downarrow = \left(\varepsilon_a \sigma T_a^4\right) V_f + \left(\varepsilon_s \sigma T_s^4\right)(1 - V_f), \quad (2.36)$$

where σ is the Stefan–Boltzmann constant, ε_a and ε_s are the emissivities of the air and surrounding surface.

Finally, outgoing longwave radiation can be calculated from:

$$L^\uparrow = \varepsilon_s \sigma T_s^4 + (1 - \varepsilon_s)L^\downarrow. \qquad (2.37)$$

Satellite thermal imagery can be used to validate and constrain energy balance modeling of surface temperature. One of the most challenging terms to evaluate analytically, but readily assessed by measurement, is $L^\downarrow$ because air temperature and emissivity vary with altitude, and the effective mean temperature of the air mass varies with elevation angle measured from the zenith. The simplest approach is to approximate $L^\downarrow$ with a single effective air temperature and a single effective emissivity, and then use field measurements to modify the evaluation. However, it will always be true that transient weather conditions other than local surface temperature, such as humidity and lapse rate, will alter downwelling sky irradiance. Like all the other terms of the energy balance, it is the integrated annual effect on ablation (hence, dominated in most regions by summer conditions) that is the most important.

2.6.2.2 Turbulent heat fluxes

Sensible and latent heat fluxes vary due to temperature and moisture gradients and atmospheric turbulence. They do not dominate over longer time periods, although latent heat flux can be of major importance for short-term ablation rates.

Modeling these components is usually done using the bulk aerodynamic expressions that characterize turbulent fluxes as:

$$Q_H = \rho_a c_p C_H \bar{u}(\bar{\theta}_z - \bar{\theta}_s) \qquad (2.38)$$

$$Q_L = \rho_a L_v C_E \bar{u}(\bar{q}_z - \bar{q}_s) \qquad (2.39)$$

where L_v is the latent heat of evaporation, $\bar{u}$ is mean wind speed, $\bar{\theta}_z$ and $\bar{\theta}_s$ are mean potential temperatures, $\bar{q}_z$ and $\bar{q}_s$ are mean specific humidities, and C_H and C_E are the exchange coefficients for heat and vapor pressure, respectively. Radiation transfer and atmospheric modeling are required to estimate spatiotemporal variability in these parameters; however, field-based measurements from point weather stations are typically used.

2.6.2.3 Ground heat

For temperate glacial ice, surface temperature is essentially zero in the daytime with nocturnal freezing. For cold glacier ice, the surface layer can be an energy sink. Surface temperature is regulated by heat conduction from englacial heat flux where the temperature gradient is a function of depth, advection, and thermal conductivity.

Sources for this energy component include geothermal heat flux, friction caused by basal sliding, and internal ice deformation. Flux across the surface can be represented as

$$Q_G = \int_0^z \rho_i c_p^i \frac{\partial T_i}{\partial t} \, dz, \qquad (2.40)$$

where $\partial T_i/\partial t$ is the rate of change in ice temperature, ρ_i is ice density, and c_p^i is the specific heat capacity of ice.

Geothermal flux is not large, except in exceptional circumstances (such as glaciers on active volcanoes), as can be appreciated by the magnitudes of global mean geothermal heat flux of about 0.08 W m^{-2}. If there exists a net mass balance driven mainly by a net loss or gain of 1% of solar constant energy flux (i.e., 13 W m^{-2}), this is over two orders of magnitude greater than geothermal flux, which therefore can be ignored except in cases of (1) polythermal ice sheets in severe polar climates, where basal melting due to geothermal flux can be a significant fraction of total mass balance, and (2) the aforementioned exceptional cases of glaciers on volcanoes, where geothermal flux can be up to three orders of magnitude greater than the global mean.

A further way to see the relative insignificance of geothermal flux is to consider that each year geothermal global mean heat flux can melt only about 8 mm of ice, which is of the order of 1% of the typical negative balances that exist for many glaciers. The frictional energy dissipation due to viscous deformation of ice and basal sliding is also generally a small term, but it can verge toward significance, as can be assessed from the total change in gravitational potential energy of a column of glacier ice as it moves downslope. Since glaciers move downslope without rapid acceleration, it must be that nearly all the gravitational potential energy is converted into frictional energy and damage to the ice crystal lattice, which ultimately is also converted to heat as the ice anneals its damage. For instance, a vertical parcel of a glacier 300 m thick moving downslope and losing 10 m elevation per year will lose potential energy per unit area at a rate of $(300 \text{ m} * 900 \text{ kg m}^{-3}) * (9.8 \text{ m s}^{-2}) * (10 \text{ m})/(3.16 * 10^7 \text{ s/yr})$ equal to 0.83 W/m^2 (i.e., about 10 times global mean geothermal flux). If the energy is completely dissipated at the bed by sliding (as an approximation to glaciers exhibiting a high degree of plug flow), this frictional energy is sufficient to melt 79 kg m^{-2} of ice per year, or about 9 cm of ice per year. This ice is melted at the bed, but presumably either infiltrates beneath the bed or is eventually expelled by basal fluid flow. This is characteristically 10% or so of the negative balances recorded for many glaciers around the world. So it is perhaps not large, but it can potentially be a term that is not completely insignificant, yet it is normally not dealt with. Changes in this energy balance term, however, can pose a stabilizing negative feedback because, as glaciers thicken and flow more rapidly, they dissipate more energy and melt more ice; whereas, when they thin and flow more slowly, they dissipate less energy and hence melt less ice.

2.6.3 Glacier mass balance modeling

Estimating glacier mass balance is complicated because ice mass gain or loss can take place at the glacier surface, within the glacier, or at the base of the glacier. At the base, loss occurs as a result of geothermal heat and sliding friction, although surface loss is most significant. Internally, mass can accumulate as meltwater refreezes and losses occur due to thermal erosion. Surface accumulation includes snowfall, wind drift, avalanches, deposition from vapor, and condensation. Surface ablation includes melting, sublimation, ice avalanches, and snow drift.

Mass balance estimates have been traditionally generated using the glaciological method, which involves inferring the mass balance from point measurements taken from ablation stakes and snow pits. Furthermore, energy balance modeling has demonstrated the significant variability in ablation caused by glacier topography and localized topographic parameters that govern shortwave and longwave energy fluxes. For alpine glaciers, topographic variation is considerable, and relief and topographic shielding significantly vary over relatively short distances. Consequently, the spatial complexity in ablation highlights the difficulty of using systematic stake measurements for accurately inferring mass balance gradients (Arnold et al. 2006).

Remote sensing and GIS permit the use of the geodetic method, wherein changes in glacier topography over a given period of time can be used to estimate volume change. Satellite-derived DEMs can be used to accomplish this. The total mass balance of a glacier (B) is:

$$B = \int_t \int_{A_s} b(x, y) \, dA_s \, dt = \rho_i \Delta V_i, \quad (2.41)$$

where A_s is the surface area of the glacier, b is the mass balance at a particular point (x, y), and dV_i is the ice volume change. This approach can be used in a GIS to compute the mean specific mass balance ($\bar{b}$) which is useful for comparing glaciers. It is computed as:

$$\bar{b} = \frac{\sum_x \sum_y \rho_i(x, y) \Delta V_i(x, y)}{A_s}. \quad (2.42)$$

Berthier et al. (2007) used this approach to estimate glacier mass balances in the western Himalaya of India. They found that remote-sensing estimates generally agreed with mass balances estimated in the field. The geodetic method, however, has its limitations including DEM accuracy and effective removal of biases (Nuth and Kääb 2011, Kääb et al. 2012).

Volume estimates also need to be corrected for the density of surface materials. Generation procedures for DEMs permit altitude accuracy in mountain environments on the order of 15–30 m (Eckert et al. 2005, Fujisada et al. 2005). Density corrections below the equilibrium line altitude (ELA) are reasonably accurate ($\sim$830–917 kg m^{-3}), although above the ELA density can vary from 50 kg m^{-3} to 830 kg m^{-3}. Finally, the point mass balance, b, cannot be determined from the geodetic method because glacier elevation is also a function of mass flux divergence and convergence due to ice flow. Consequently, numerical flow modeling must also be used to relate results from the two methods in detail.

Hubbard et al. (2000) described the use of the mass continuity equation to compute mass balance such that:

$$b(x, y) = \frac{\partial h_i(x, y)}{\partial t} + \nabla \cdot [H_i(x, y) \bar{v}(x, y)], \quad (2.43)$$

where h_i is ice elevation of the glacier surface, H_i is ice thickness, $\bar{v}$ is the vertically averaged ice velocity vector, and ∇ is the horizontal divergence operator. The term, $\partial h_i / \partial t$, can be determined from the geodetic method, while the local mass flux term can be derived from numerical three-dimensional ice flow modeling or surface ice velocity fields generated using feature tracking. Their results demonstrated that this approach has potential for deriving high spatial and temporal resolution estimates of mass balance, the main limitation being in the accurate characterization of basal sliding.

2.7 CONCLUSIONS

Remote-sensing science and technology are indispensable for assessing ice sheets and alpine glaciers, as thematic and quantitative estimates of glacier parameters can be derived from satellite imagery in the reflective and thermal regions of the spectrum. Space-based, change detection studies based upon spectral and topographic information are providing estimates of glacier fluctuations around the world. Unfortunately, systematic inventories of other important glacier parameters, such as supraglacial debris characteristics, lakes, glacier features, and velocity fields have yet to be effectively realized due to a variety of factors. Image information content, the complexity of the radiation transfer cascade, and new analytical approaches provide the basis for new opportunities for information extraction. These include improved mapping capabilities using reflectance anisotropy, scale-dependent spatial analysis, and data fusion for characterization of glacier surfaces. Existing work, coupled with new developments, will provide us with more empirical data that will provide new insights into explaining glacier fluctuations.

Interpreting the causal mechanisms responsible for glacier fluctuations requires more sophisticated analysis that integrates remote-sensing science and technology with deterministic modeling. Climate, surface energy budget, ice flow, and glacier modeling are required in order to assess glacier dynamics and mass balance. Only in this way can a multitude of internal and external forcing factors and interrelated processes be evaluated objectively to quantitatively ascertain glacier response to climate change. We can then generate more reliable estimates of regional mass balance trends and improve estimates of the contribution of melting ice sheets and alpine glaciers to rising sea level.

2.8 ACKNOWLEDGMENTS

2.9   NOTATION

a_p Water absorption coefficient [dimensionless]

$A_\odot$ Area of the solar disk [km^2]

A_s Surface area of a glacier [km^2]

A_p Pixel area [m^2]

b Mass balance of a glacier at a particular point (x,y), water equivalent [mm]

$\bar{b}$ Mean specific mass balance, water equivalent [mm]

b_p Water scattering coefficient [dimensionless]

B Total mass balance of a glacier, water equivalent [mm]

c_p Atmospheric specific heat at constant pressure [J kg^{-1} K^{-1}]

c_p^i Specific heat capacity of ice [J kg^{-1} K^{-1}]

C Concentration of particles in water [mg L^{-1}]

C_E Vapor–pressure exchange coefficient

C_H Heat exchange coefficient

C_1 First radiation constant, 3.74151×10^8 [W m^{-2}μm^4]

C_2 Second radiation constant, 1.43879×10^4 [μm K]

d Distance [m]

d_{es} Earth–Sun distance [km]

E^0 Exoatmospheric spectral irradiance [W m^{-2}μm^{-1}]

E Surface spectral irradiance [W m^{-2}μm^{-1}]

E_a Diffuse skylight aerosol-scattered spectral irradiance [W m^{-2}μm^{-1}]

E_t Adjacent terrain spectral irradiance [W m^{-2}μm^{-1}]

E_b Direct beam spectral irradiance [W m^{-2}μm^{-1}]

E_d Diffuse skylight spectral irradiance [W m^{-2}μm^{-1}]

E_g Diffuse skylight ground-backscattered spectral irradiance [W m^{-2}μm^{-1}]

E_r Diffuse skylight Rayleigh-scattered spectral irradiance [W m^{-2}μm^{-1}]

E_t Total surface irradiance [W m^{-2}]

E_v Evaporation rate [kg day^{-1}]

f_p Scattering phase function [dimensionless]

f_r Bidirectional reflectance distribution function [sr^{-1}]

F_x Atmospheric frictional term for the x direction

F_y Atmospheric frictional term for the y direction

F_z Atmospheric frictional term for the z direction

g Gravitational acceleration [m s^{-2}]

h Thickness [m]

h_i Glacier ice altitude [m]

H Atmospheric heating term [W m^{-2}]

H_i Ice thickness [m]

H_d Debris depth [m]

i Incidence angle of illumination

k Thermal conductivity [W m^{-1} K^{-1}]

L Shortwave reflected surface radiance [W m^{-2}μm^{-1} sr^{-1}]

$L_\uparrow$ Longwave surface radiance [W m^{-2}μm^{-1} sr^{-1}]

L^0 At-satellite measured shortwave spectral radiance [W m^{-2}μm^{-1} sr^{-1}]

$L_\uparrow^0$ At-satellite measured longwave spectral radiance [W m^{-2}μm^{-1} sr^{-1}]

$L^\downarrow$ Total longwave sky irradiance [W m^{-2}]

$L_t^\downarrow$ Longwave spectral irradiance from adjacent terrain [W m^{-2}μm^{-1}]

$L^\uparrow$ Total emitted longwave radiation [W m^{-2}]

$L_p^\uparrow$ Upwelling longwave atmospheric path radiance [W m^{-2}μm^{-1} sr^{-1}]

L_f Latent heat of fusion for ice [J kg^{-1}]

L_p Additive path radiance [W m^{-2}μm^{-1} sr^{-1}]

L_v Latent heat of evaporation [J kg^{-1}]

M Spectral exitance [W m^{-2}μm^{-1}]

M_a Ablation rate [mm day^{-1}]

p Atmospheric pressure [mb]

P Precipitation rate [cm yr^{-1}]

q Specific humidity [kg kg^{-1}]

$\bar{q}_s$ Mean specific humidity at surface [kg kg^{-1}]

$\bar{q}_z$ Mean specific humidity at altitude z [kg kg^{-1}]

Q_C Conductive heat flux through the debris [W m^{-2}]

Q_N Net radiation flux [W m^{-2}]

Q_H Sensible heat flux [W m^{-2}]

Q_L Latent heat flux [W m^{-2}]

Q_G Ground heat flux [W m^{-2}]

Q_R Sensible heat flux from rain [W m^{-2}]

Q_M Melting energy [W m^{-2}]

R Dry-air gas constant [m^3 mb kg^{-1} K^{-1}]

R_r Bidirectional reflectance factor [dimensionless]

R_t Thermal resistance of debris [m^2 K W^{-1}]

S Cast shadow binary coefficient [dimensionless]

t Time

$T_\odot$ Temperature of the Sun [K]

T_a Temperature of atmosphere [K]

T_i Temperature of ice [K]

T_s Temperature of surface [K]

T_t Temperature of the adjacent terrain [K]

$\mathbf{T}$ Transmission coefficient [dimensionless]

$\mathbf{T}^{\downarrow}$ Total downward atmospheric transmittance coefficient [dimensionless]

$\mathbf{T}^{\uparrow}$ Total upward atmospheric transmittance coefficient [dimensionless]

$\mathbf{T}_r$ Rayleigh atmospheric transmittance coefficient [dimensionless]

$\mathbf{T}_a$ Aerosol atmospheric transmittance coefficient [dimensionless]

$\mathbf{T}_{O_3}$ Ozone atmospheric transmittance coefficient [dimensionless].

$\mathbf{T}_{gas}$ Miscellaneous gases atmospheric transmittance coefficient [dimensionless]

$\mathbf{T}_{H_2O}$ Water vapor atmospheric transmittance coefficient [dimensionless]

$\bar{u}$ Mean wind speed [m s^{-1}]

U Zonal wind speed [m s^{-1}]

$\bar{v}$ Vertically averaged ice velocity vector

V Meridional wind speed [m s^{-1}]

V_f Hemispherical sky view factor coefficient [dimensionless]

V_i Glacier ice volume [m^{-3}]

W Vertical wind speed [m s^{-1}]

x Horizontal cartesian coordinate (longitude direction)

y Horizontal cartesian coordinate (latitude direction)

z Vertical cartesian coordinate (altitude direction)

α Surface albedo [dimensionless]

α_a Surface absorption coefficient [dimensionless]

α_{psa} Planar surface albedo [dimensionless]

α_{ssa} Spherical surface albedo [dimensionless]

α_{te} Atmospheric thermal expansion coefficient

ε_s Surface emissivity [dimensionless]

ε_a Atmospheric emissivity [dimensionless]

θ_i Incident solar zenith angle

θ_{max} Maximum local horizon angle

θ_r Reflected zenith angle

θ_t Terrain slope angle

$\bar{\theta}_s$ Mean potential temperature at surface [K]

$\bar{\theta}_z$ Mean potential temperature at altitude z [K]

λ Wavelength [μm]

π Pi constant

ρ Reflectance [dimensionless]

ρ_a Density of atmosphere [kg m^{-3}]

ρ_i Density of ice [kg m^{-3}]

ρ_w Density of water [kg m^{-3}]

σ Stefan–Boltzmann constant [W m^{-2} K^{-4}]

τ Extinction coefficient

φ Latitude [radians]

ϕ_i Incident solar azimuth angle

ϕ_r Reflected azimuth angle

ϕ_t Slope–aspect angle of the terrain

Ω Angular velocity of the Earth [rad s^{-1}]

ω Single-scattering albedo [dimensionless]

∇ Horizontal divergence operator

2.10 REFERENCES

Aniya, M., Sato, H., Naruse, R., Skvarca, P., Casassa, G. (1996) The use of satellite and airborne imagery to inventory outlet glaciers of the southern Patagonia icefield, South America. *Photogrammetric Engineering and Remote Sensing*, **62**(12), 1361–1369.

Arendt, A. (1999) Approaches to modelling the surface albedo of a high Arctic glacier. *Geografiska Annaler*, **81A**(4), 477–488.

Arnold, N.S., Rees, W.G., Hodson, A.J., Kohler, J. (2006) Topographic controls on the surface energy balance of a high Arctic valley glacier. *Journal of Geophysical Research*, **111**, F02011, doi: 10.1029/2005JF000426.

Bamber, L.L., and Kwok, R. (2004) Remote-sensing techniques. In: J.L. Bamber and A.J. Payne (Eds.), *Mass Balance of the Cryosphere: Observations and Modelling of Contemporary and Future Changes*. Cambridge University Press, Cambridge, U.K., pp. 59–113.

Bamber, J.L., and Payne, A.J. (2004) *Mass Balance of the Cryosphere: Observations and Modelling of Contemporary and Future Changes*. Cambridge University Press, Cambridge, U.K.

Barry, R.G. (2006) The status of research on glaciers and global glacier recession: A review. *Progress in Physical Geography*, **30**(3), 285–306.

Benn, D.I., and Evans, D.J.A. (1998) *Glaciers and Glaciation*, Arnold, London.

Benson, C.S. (1996) *Stratigraphic Studies in the Snow and Firn of the Greenland Ice Sheet* (Tech. Rep. 70), U.S. Army Cold Regions Research and Engineering Laboratory, Hanover, NH.

Berthier, E., Arnaud, Y., Rajesh, K., Sarfaraz, A., Wagnon, P., and Chevallier, P. (2007) Remote sensing estimates of glacier mass balances in the Himachal Pradesh (Western Himalaya, India). *Remote Sensing of Environment*, **108**(3), 327–338.

Bishop, M.P., Shroder, J.F., Jr., and Ward, J.L. (1995) SPOT multispectral analysis for producing supraglacial debris-load estimates for Batura Glacier, Pakistan. *Geocarto International*, **10**(4), 81–90.

Bishop, M.P., Shroder, Jr., J.F., Hickman, B.L., and Copland, L. (1998) Scale dependent analysis of satellite imagery for characterization of glacier surfaces in the Karakoram Himalaya. *Geomorphology*, **21**, 217–232.

Bishop, M.P., Shroder, Jr., J.F., and Hickman, B.L. (1999) High resolution satellite imagery and neural networks for information extraction in a complex mountain environment. *Geocarto International*, **14**(2), 17–26.

Bishop, M.P., Bonk, R., Kamp, U., Jr., and Shroder, J.F., Jr. (2001) Terrain analysis and data modeling for alpine glacier mapping. *Polar Geography*, **24**(4), 257–276.

Bishop, M.P., Shroder, J.F., Jr., Bonk, R., and Olsenholler, J. (2002) Geomorphic change in high mountains: A western Himalayan perspective. *Global and Planetary Change*, **32**, 311–329.

Bishop, M.P., Barry, R.G., Bush, A.B.G., Copland, L., Dwyer, J.L., Fountain, A.G., Haeberli, W., Hall, D.K., Kääb, A., Kargel, J.S. et al. (2004a). Global land-ice measurements from space (GLIMS): Remote sensing and gis investigations of the Earth's cryosphere. *Geocarto International*, **19**(2), 57–84.

Bishop, M.P., Colby, J.D., Luvall, J.C., Quattrochi, D., and Rickman, D.L. (2004b). Remote-sensing science and technology for studying mountain environments. In: M.P. Bishop and J.F. Shroder, Jr. (Eds.), *Geographic Information Science and Mountain Geomorphology*, Springer/Praxis, Heidelberg, Germany/Chichester, U.K., pp. 147–187.

Bush, A.B.G. (2000) A positive feedback mechanism for Himalayan glaciation. *Quaternary International*, **65**(6), 3–13.

Bush, A.B.G. (2001) Pacific sea surface temperature forcing dominates orbital forcing of the early Holocene monsoon. *Quaternary Research*, **55**, 25–32.

Carrivick, J.L., and Brewer, T.R. (2004) Improving local estimations and regional trends of glacier Equilibrium Line Altitudes. *Geografiska Annaler*, **86A**(1), 67–79.

Chavez, P.S., Jr. (1996) Image-based atmospheric corrections: Revisited and improved. *Photogrammetric Engineering and Remote Sensing*, **62**(9), 1025–1036.

Choudhury, B.J., and Chang, A.T.C. (1979) Two-stream theory of reflectance of snow. *IEEE Transactions on Geoscience and Remote Sensing*, **GE–17**(3), 63–68.

Comiso, J.C. (2006) Arctic warming signals from satellite observations. *Weather*, **61**(3), 70–76.

Diner, D.J., Asner, G.P., Davies, R., Knyazikhin, Y., Muller, J.P., Nolin, A.W., Pinty, B., Schaaf, C.B., and Stroeve, J. (1999) New directions in Earth observing: Scientific application of multi-angle remote sensing. *Bulletin of the American Meteorological Society*, **80**, 2209–2228.

Dozier, J. (1989) Spectral signature of alpine snow cover from the Landsat Thematic Mapper. *Remote Sensing of the Environment*, **28**, 9–22.

Dozier, J., Bruno, J., and Downey, P. (1981) A faster solution to the horizon problem. *Computers and Geosciences*, **7**(1), 145–151.

Dyurgerov, M.B., and Meier, M.F. (2004) Glaciers and the study of climate and sea-level change. In: J.L. Bamber and A.J. Payne (Eds.), *Mass Balance of the Cryosphere: Observations and Modelling of Contemporary and Future Changes*. Cambridge University Press, Cambridge, U.K., pp. 579–621.

Eckert, S., Kellenberger, T., and Itten, K. (2005) Accuracy assessment of automatically derived digital elevation models from Aster data in mountainous terrain. *International Journal of Remote Sensing*, **26**(9), 1943–1957.

Feng, F.X., Schott, J.R., and Gallagher, T.W. (1993) Comparison of methods for generation of absolute reflectance factor values for BRDF studies. *Applied Optics*, **32**(7), 1234–1242.

Fournier, G.R., and Fourand, J.L. (1994) Analytic phase function for ocean water. In: J.S. Jaffe (Ed.), *Ocean Optics XII*. International Society for Optics and Photonics, Bellingham, WA, pp. 194–201.

Fujisada, H., Bailey, G.B., Kelly, G.G., Hara, S., and Abrams, M.J. (2005) ASTER DEM performance. *IEEE Transactions on Geoscience and Remote Sensing*, **43**(12), 2707–2714.

Furbish, D.J., and Andrews, J.T. (1984) The use of hypsometry to indicate long-term stability and response of valley glaciers to changes in mass transfer. *Journal of Glaciology*, **30**(105), 199–211.

Ganapol, B.D., and Furfaro, R. (2008) *The Art of Analytical Benchmarking* (Lecture Notes in Computational Science and Engineering No. 62), Springer, New York, pp. 105–134.

Gardner, J.S., and Jones, N.K. (1993) Sediment transport and yield at the Raikot Glacier, Nanga Parbat, Punjab Himalaya. In: J.F. Shroder Jr. (Ed.), *Himalaya to the Sea: Geology, Geomorphology and the Quaternary*, Routledge, London, pp. 184–197.

Giles, P.T. (2001) Remote sensing and cast shadows in mountainous terrain. *Photogrammetric Engineering and Remote Sensing*, **67**(7), 833–839.

Gillespie, A.R., Cothern, J.S., Matsunaga, T., Rokugawa, S., and Hook, S.J. (1998) Temperature and emissivity separation from Advanced Spaceborne Thermal Emission and Reflection Radiometer (ASTER) images. *IEEE Transactions on Geoscience and Remote Sensing*, **36**, 1113–1126.

Gratton, D.J., Howarth, P.J., and Marceau, D.J. (1990) Combining DEM parameters with Landsat MSS and TM imagery in a GIS for mountain glacier characterization. *IEEE Transactions on Geoscience and Remote Sensing*, **GE–28**, 766–769.

Grenfell, T.C., and Perovich, D.K. (1981) Radiation absorption coefficients of polycrystalline ice from 400–1400 nm. *Journal of Geophysical Research*, **86**(C8), 7447–7450.

Greuell, W., and de Wildt, M. (1999) Anisotropic reflection by melting glacier ice: Measurements and parametrizations in Landsat TM bands 2 and 4. *Remote Sensing of Environment*, **70**, 265–277.

Gueymard, C. (1995) *SMARTS2, A Simple Model of the Atmospheric Radiative Transfer of Sunshine: Algorithms and Performance Assessment* (Tech. Rep. FSEC-PF-270-95), Florida Solar Energy Center, Cocoa, FL.

Haeberli, W. (1998) Historical evolution and operational aspects of worldwide glacier monitoring. In: W. Haeberli, M. Hoelzle, and S. Suter (Eds.) (1998) *Into the Second Century of Worldwide Glacier Monitoring: Prospects and Strategies*, UNESCO, Paris, pp. 35–47.

Haeberli, W. (2004) Glacier and ice caps: Historical background and strategies of world-wide monitoring. In: J.L. Bamber and A.J. Payne (Eds.), *Mass Balance of the Cryosphere: Observations and Modelling of Contemporary and Future Changes*. Cambridge University Press, Cambridge, U.K., pp. 559–578.

Haeberli, W., and Beniston, M. (1998) Climate change and its impacts on glaciers and permafrost in the Alps. *Ambio*, **27**(4), 258–265.

Haeberli, W., and Hoelzle, M. (1995) Application of inventory data for estimating characteristics of and regional climate-change effects on mountain glaciers: A pilot study with the European Alps. *Annals of Glaciology*, **21**, 206–212.

Haeberli, W., Hoelzle, M., and Suter, S. (Eds.) (1998) *Into the Second Century of Worldwide Glacier Monitoring: Prospects and Strategies*, UNESCO, Paris.

Hall, D.K., and Riggs, G.A. (2007) Accuracy assessment of the MODIS snow-cover products. *Hydrological Processes*, **21**(12), 1534–1547, doi: 10.1002/hyp.6715.

Hall, D.K., Chang, A.T.C., Foster, J.L., Benson, C.S., and Kovalick, W.M. (1989) Comparison of in situ and Landsat derived reflectance of Alaskan glaciers. *Remote Sensing of the Environment*, **28**, 23–31.

Hall, D.K., Bayr, K.J., Schöner, W., Bindschadler, R.A., and Chien, J.Y.L. (2003) Consideration of the errors inherent in mapping historical glacier positions in Austria from the ground and space (1893–2001). *Remote Sensing of Environment*, **86**(4), 566–577.

Hall, D.K., Kelly, R.E.J., Foster, J.L., and Chang, A.T.C. (2005) *Encyclopedia of Hydrologic Sciences*, John Wiley & Sons, Chichester, U.K.

Hall, D.K., Williams, R.S., Jr., Casey, K.A., DiGirolamo, N.E., and Wan, Z. (2006) Satellite-derived, melt-season surface temperature of the Greenland Ice Sheet (2000–2005) and its relationship to mass balance. *Geophysical Research Letters*, **33**, L11501, doi: 10.1029/2006GL026444.

Hansen, J.E., and Travis, L.D. (1974) Light scattering in planetary atmospheres. *Space Science Review*, **16**, 527–610.

Hock, R. (2005) Glacier melt: A review of processes and their modelling. *Progress in Physical Geography*, **29**(3), 362–391.

Hubbard, A., Willis, I., Sharp, M., Mair, D., Nienerow, P., Hubbard, B., and Blatter, H. (2000) Glacier mass-balance determination by remote sensing and high-resolution modelling. *Journal of Glaciology*, **46**(154), 491–498.

Jansson, P. (1996) Dynamics and hydrology of small polythermal valley glacier. *Geografiska Annaler*, **78A**(2/3), 171–180.

Kääb, A. (2005a) Combination of SRTM3 and repeat ASTER data for deriving alpine glacier flow velocities in the Bhutan Himalaya. *Remote Sensing of Environment*, **94**, 463–474.

Kääb, A. (2005b) *Remote Sensing of Mountain Glaciers and Permafrost Creep* (Vol. 48 of Physical Geography Series), Geographisches Institut der Universität, Zurich.

Kääb, A., Berthier, E., Nuth, C., Gardelle, J., and Arnaud, Y. (2012) Contrasting patterns of early

twenty-first-century glacier mass change in the Himalayas. *Nature*, **488**, 495–498.

Kargel, J.S., Abrams, M.J., Bishop, M.P., Bush, A., Hamilton, G., Jiskoot, H., Kääb, A., Kieffer, H.H., Lee, E.M., Paul, F. et al. (2005) Multispectral imaging contributions to global land ice measurements from space. *Remote Sensing of the Environment*, **99**, 187–219.

Khalsa, S.J.S., Dyurgerov, M.B., Khromova, T., Raup, B.H., and Barry, R.G. (2004) Space-based mapping of glacier changes using ASTER and GIS tools. *IEEE Transactions on Geoscience and Remote Sensing*, **42**, 2177–2182.

Klein, A.G., and Stroeve, J. (2002) Development and validation of snow albedo algorithm for the MODIS instrument. *Annals of Glaciology*, **34**, 45–52.

Knap, W.H., and Oerlemans, J. (1996) The surface albedo of the Greenland Ice Sheet: Satellite-derived and in situ measurements in the Søndre Strømfjord area during the 1991 melt season. *Journal of Glaciology*, **42**(141), 364–374.

König, M., Winther, J.G., and Isaksson, E. (2001) Measuring snow and glacier ice properties from satellite. *Reviews of Geophysics*, **39**, 1–27.

Kotlyakov, V.M., Serebrjanny, L.R., and Solomina, O.N. (1991) Climate change and glacier fluctuations during the last 1,000 years in the southern mountains of the USSR. *Mountain Research and Development*, **11**, 1–12.

Kulkarni, A.V. (1992). Mass balance of Himalayan glaciers using AAR and ELA methods. *Journal of Glaciology*, **38**, 101–104.

Kulkarni, A.V., Rathore, B.P., and Alex, S. (2004) Monitoring of glacier mass balance in the Baspa basin using accumulation area ratio method. *Current Science*, **86**(1), 185–190.

Loomis, S.R. (1970) Morphology and ablation processes on glacier ice. *Proceedings of the Association of American Geographers*, **2**, 88–92.

Lu, D., Mausel, P., Brondzio, E., and Moran, E. (2004) Change detection techniques. *International Journal of Remote Sensing*, **25**(12), 2365–2401.

MacClune, K.L., Fountain, A.G., Kargel, J.S., and MacAyeal, D.R. (2003) Glaciers of the McMurdo dry valleys: Terrestrial analog for Martian polar sublimation. *Journal of Geophysical Research*, **108**(E4), 5031–5043.

Maisch, M. (2000) The longterm signal of climate change in the Swiss Alps: Glacier retreat since the end of the Little Ice Age and future ice decay scenarios. *Geografia Fisica e Dinamica Quaternaria*, **23**(2), 139–151.

Mark, B.G., Harrison, S.P., Spessa, A., New, M., Evans, D.J.A., Helmens, K.F. (2005) Tropical snowline changes at the Last Glacial Maximum: A global assessment. *Arctic and Alpine Research*, **138/139**, 168–201.

Mattson, L.E., Gardner, J.S., and Young, G.J. (1993) Ablation on debris covered glaciers: An example from the Rakhiot Glacier, Punjab, Himalaya. In: *Snow and Ice Hydrology* (No. 218), International Association of Hydrological Sciences, Rennes, France.

McClung, D.M., and Armstrong, R.L. (1993) Temperate glacier time response from field data. *Journal of Glaciology*, **39**(132), 323–326.

Meier, M.F., and Wahr, J.M. (2002) Sea level is rising: Do we know why? *Proceedings of the National Academy of Science*, **99**(10), 6524–6526.

Meierding, T.C. (1982) Late Pleistocene glacier equilibrium-line in the Colorado Front Range: A comparison of methods. *Quaternary Research*, **18**, 289–310.

Mishchenko, M.M., Dlugach, J.M., Yanovitskij, E.G., and Zakharova, E.T. (1999) Bidirectional reflectance of flat, optically thick particulate layers: An efficient radiative transfer solution and applications to snow and soil surfaces. *Journal of Quantitative Sectroscopy and Radiative Transfer*, **63**, 409–432.

Molnar, P., and England, P. (1990) Late Cenozoic uplift of mountain ranges and global climate change: Chicken or egg? *Nature*, **346**, 29–34.

Nakawo, M., and Young, G.J. (1981) Field experiments to determine the effect of a debris layer on ablation of glacier ice. *Annals of Glaciology*, **2**, 85–91.

Nakawo, M., and Rana, B. (1999) Estimate of ablation rate of glacier ice under a supraglacial debris layer. *Geografiska Annaler*, **81A**, 695–701.

Nakawo, M., Morohoshi, T., and Uehara, S. (1993) Satellite data utilization for estimating ablation of debris covered glaciers. Paper No. 218 presented at *Snow and Glacier Hydrology: Proceedings of the Kathmandu Symposium*, IAHS Press, Wallingford, U.K., pp. 75–83.

Nesje, A. (1992) Topographical effects on the equilibrium line altitude on glaciers. *Geojournal*, **27**, 383–391.

Nienow, P.W., Hubbard, A.L., Hubbard, B.P., Chandler, D.M., Mair, D.W.F., Sharp, M.J., and Willis, I.C. (2005) Hydrological controls on diurnal ice flow variability in valley glaciers. *Journal of Geophysical Research*, **110**(F4), F04002.1–F04002.11.

Nolin, A.W., and Liang, S. (2000) Progress in bi-directional reflectance modeling and applications for surface particulate media: Snow and soils. *Remote Sensing Reviews*, **18**, 307–342.

Nolin, A.W., and Stroeve, J.C. (1997) The changing albedo of the Greenland Ice Sheet: Implications for climate change. *Annals of Glaciology*, **25**, 51–57.

Nuth, C., and Kääb, A. (2011) Co-registration and bias corrections of satellite elevation data sets for quantifying glacier thickness change. *The Cryosphere*, **5**(1), 271–290.

Osmaston, H. (2005) Estimates of glacier equilibrium line altitudes by the Area × Altitude, the Area × Altitude Balance Ratio and the Area × Altitude Balance Index methods and their validation. *Quaternary International*, **138/139**, 22–31.

Paul, F., Kääb, A., Maisch, M., Kellenberger, T., and Haeberli, W. (2002) The new remote sensing derived

Swiss glacier inventory: I. Methods. *Annals of Glaciology*, **34**, 355–361 (*Fourth International Symposium on Remote Sensing in Glaciology*).

Paul, F., Huggel, C., and Kääb, A. (2004) Combining satellite multispectral image data and a digital elevation model for mapping debris-covered glaciers. *Remote Sensing of Environment*, **89**, 510–518.

Petzold, T.J. (1972) *Volume Scattering Functions for Selected Ocean Waters* (Tech. Rep. SIO Ref 71-78), Scripps Institution of Oceanography, San Diego, CA

Prieur, L., and Sathyendranath, S. (1981) An optical classification of coastal and oceanic waters based on the specific absorption of phyplankton pigments, dissolved organic matter, and other particulate materials. *Limnology and Oceanography*, **26**, 671–689.

Proy, C., Tanre, D., and Deschamps, P.Y. (1989) Evaluation of topographic effects in remotely sensed data. *Remote Sensing of the Environment*, **30**, 21–32.

Ramsay, B. (1998) The interactive multisensor snow and ice mapping system. *Hydrological Processes*, **12**, 1537–1546.

Raup, B., Kääb, A., Kargel, J.S., Bishop, M.P., Hamilton, G., Lee, E.M., Paul, F., Rau, F., Soltesz, D., Khalsa, S.J. et al. (2007) Remote sensing and GIS technology in the Global Land Ice Measurements from Space (GLIMS) Project. *Computers and Geosciences*, **33**, 104–125.

Rees, W.G. (2006) *Remote Sensing of Snow and Ice*, Taylor & Francis, Boca Raton, FL.

Robinson, D.A., and Kukla, G. (1985) Maximum surface albedo of seasonally snow-covered lands in the Northern Hemisphere. *Journal of Climate and Applied Meteorology*, **24**, 402–411.

Rossi, R.E., Dungan, J.L., and Beck, L.R. (1994) Kriging in the shadows: Geostatistical interpolation for remote sensing. *Remote Sensing of the Environment*, **49**, 32–40.

Ruddiman, W. F. (Ed.) (1997) *Tectonic Uplift and Climate Change*. Plenum Press, New York.

Scambos, T.A., Dutkiewicz, M.J., Wilson, J.C., and Bindschadler, R.A. (1992) Application of image cross-correlation to the measurement of glacier velocity using satellite image data. *Remote Sensing of Environment*, **42**(3), 177–186.

Schaaf, C.B., and 21 others (2002) First operational BRDF, albedo nadir reflectance products from MODIS. *Remote Sensing of Environment*, **83**(1/2), 135–148.

Seltzer, G.O. (1993) Late-Quaternary glaciation as a proxy for climate change in the central Andes. *Mountain Research and Development*, **13**, 129–138.

Shroder, J.F., Jr., and Bishop, M.P. (2000) Unroofing of the Nanga Parbat Himalaya. In: M.A. Khan, P.J. Treloar, M.P. Searle, and M.Q. Jan (Eds.), *Tectonics of the Nanga Parbat Syntaxis and the Western Himalaya* (No. 170 in Special Publication), Geological Society, London, pp. 163–179.

Siewert, C.E. (2000) A concise and accurate solution to Chandrasekhars basic problem in radiative transfer. *Journal of Quantitative Sectroscopy and Radiative Transfer*, **64**, 109–130.

Stroeve, J., and Nolin, A. (2002) New methods to infer snow albedo from the MISR instrument with applications to the Greenland Ice Sheet. *IEEE Transactions on Geoscience and Remote Sensing*, **40**(7), 1616–1625.

Stroeve, J., Nolin, A., and Steffen, K. (1997) Comparison of AVHRR-derived and in situ surface albedo over the Greenland Ice Sheet. *Remote Sensing of Environment*, **62**, 262–276.

Stroeve, J., Box, J., and Haran, T. (2006) Evaluation of MODIS (MOD10A1) daily snow albedo product over the Greenland Ice Sheet. *Remote Sensing of Environment*, **105**, 155–171.

Torsnes, I., Rye, N., and Nesje, A. (1993) Modern and Little Ice Age equilibrium line altitudes on outlet valley glaciers from Jostedalsbreen, Western Norway: An evaluation of different approaches to their calculation. *Arctic and Alpine Research*, **25**, 106–116.

Warren, S.G. (1982) Optical properties of snow. *Reviews of Geophysics and Space Physics*, **20**(1), 67–89.

Warren, S.G., Brandt, R.E., and O'Rawe, H.P. (1998) Effect of surface roughness on bidirectional reflectance of Antarctic snow. *Journal of Geophysical Research*, **103**(E11), 25789–25807.

Williams, R.S., Hall, D.K., and Benson, C.S. (1991) Analysis of glacier facies using satellite techniques. *Journal of Glaciology*, **37**(125), 120–128.

Winther, J.G. (1993) Landsat TM derived and in-situ summer reflectance of glaciers in Svalbard. *Polar Research*, **12**, 37–55.

Zeitler, P.K., Meltzer, A.S., Koons, P.O., Craw, D., Hallet, B., Chamberlain, C.P., Kidd, W.S., Park, S.K., Seeber, L., Bishop, M.P. et al. (2001) Erosion, Himalayan geodynamics, and the geomorphology of metamorphism. *GSA Today*, **11**, 4–8.

Zemp, M., Haeberli, W., Hoelzle, M., and Paul, F. (2006) Alpine glaciers to disappear within decades? *Geophysical Research Letters*, **33**, L13504, doi: 10.1029/2006GL026319.

Zwally, H.J., Abdalati, W., Herring, T., Larson, K., Saba, J., and Steffen, K. (2002) Surface melt-induced acceleration of Greenland ice-sheet flow. *Science*, **297**(5579), 218–222.